













Calibrating Photometric Mid-Infrared Star Formation Rates for JWST

STACEY ALBERTS ^{1,2} GEORGE H. RIEKE ² IRENE SHIVAEI ³ ZHIYUAN JI ² PASCAL OESCH,^{4,5,6} GABRIEL BRAMMER,^{5,6}
JAKOB M. HELTON ⁷ JIANWEI LYU (吕建伟) ² ERICA J. NELSON,⁸ NAVEEN REDDY ⁹ PIERLUIGI RINALDI ¹⁰
YANG SUN ² KATHERINE E. WHITAKER ^{11,12} CHRISTINA C. WILLIAMS ¹³ CHRISTOPHER N. A. WILLMER ² AND
STIJN WUYTS¹⁴

¹AURA for the European Space Agency (ESA), Space Telescope Science Institute, 3700 San Martin Dr., Baltimore, MD 21218, USA

²Steward Observatory, University of Arizona, 933 North Cherry Avenue, Tucson, AZ 85719, USA

³Centro de Astrobiología (CAB), CSIC-INTA, Ctra. de Ajalvir km 4, Torrejón de Ardoz, E-28850, Madrid, Spain

⁴Department of Astronomy, University of Geneva, Chemin Pegasi 51, 1290 Versoix, Switzerland

⁵Niels Bohr Institute, University of Copenhagen, Lyngbyvej 2, DK2100 Copenhagen, Denmark

⁶Cosmic Dawn Center (DAWN), Copenhagen, Denmark

⁷Department of Astronomy & Astrophysics, The Pennsylvania State University, University Park, PA 16802, USA

⁸Department for Astrophysical and Planetary Science, University of Colorado, Boulder, CO 80309, USA

⁹Department of Physics and Astronomy, University of California, Riverside, 900 University Avenue, Riverside, CA 92521, USA

¹⁰Space Telescope Science Institute, 3700 San Martin Drive, Baltimore, Maryland 21218, USA

¹¹Department of Astronomy, University of Massachusetts, Amherst, MA 01003, USA

¹²Cosmic Dawn Center (DAWN), Denmark

¹³NSF National Optical-Infrared Astronomy Research Laboratory, 950 North Cherry Avenue, Tucson, AZ 85719, USA

¹⁴Department of Physics, University of Bath, Claverton Down, Bath, BA2 7AY, UK

ABSTRACT

The mid-infrared (mid-IR) spectrum in galaxies has a long history as a valuable proxy for the dust-obscured component of the star formation rate (SFR) in massive galaxies. In this work, we exploit the capabilities of the James Webb Space Telescopes (JWST) to expand our understanding of the mid-IR and its use in measuring SFRs, covering four orders of magnitude in total infrared luminosity ($9 \lesssim \log L_{\text{IR}}/L_{\odot} \lesssim 13$). First, using a Main Sequence sample at $1 < z < 1.75$ from SMILES, we calibrate mid-IR-based SFRs against the Pa α emission line – a gold standard SFR indicator – from the FRESCO survey. We find that the rest-frame $\sim 6 - 8 \mu\text{m}$ emission – dominated by PAHs and probed by the Mid-Infrared Instrument (MIRI) at $z \sim 1.3$ – has a superlinear relation with $\text{SFR}_{\text{Pa}\alpha}$ below $\sim 8 M_{\odot} \text{ yr}^{-1}$, in sharp contrast with the unity relation in more massive galaxies. We derive SFR calibrations for MIRI photometry, finding that a single, representative IR template improves the scatter. We additionally calibrate a UV+IR composite indicator, assuming energy balance, which does return a unity relation, with low scatter. Our examination of the mid-IR in our MS sample indicates that it is tracking the global obscuration fraction, making it a robust proxy for SFR down to our low mass end, $\log M_{\star}/M_{\odot} \sim 9$, and across the redshift range where MIRI probes the PAHs ($0.3 \lesssim z \lesssim 3$). Finally, we examine the bright end not represented in SMILES, comparing the behavior of local and cosmic noon ultra luminous infrared galaxies to show that the robustness of using the IR as a SFR proxy extends from the faint to bright regimes.

Keywords: Star formation (1569) – Polycyclic aromatic hydrocarbons (1280) – James Webb Space Telescope (2291) – Infrared galaxies(790), Astronomical techniques: Calibration (2179)

1. INTRODUCTION

Our understanding of galaxy evolution hinges on accurately quantifying the rate of formation of new stars in galaxies across cosmic time. As such, a substantial amount of time and effort has gone into assessing observables from the X-ray

to the radio as star formation rate (SFR) indicators (see [Kennicutt & Evans 2012](#), for a review). Direct tracers of high energy ionizing or non-ionizing continuum photons such as the Balmer lines or the ultraviolet (UV), respectively, are directly proportional to the emission from young stars. However, their use is often compromised by absorption or scattering from cosmic dust (e.g., [Cardelli et al. 1989](#); [Gordon et al. 1997](#); [Calzetti et al. 2000](#); [Reddy et al. 2008](#)). This

has spurred the use of indirect tracers such as the infrared to obtain a complete and unbiased accounting of recent star formation.

The dominant absorbing medium, cosmic dust, is an important constituent in a galaxy’s ecosystem; it both influences and is influenced by the physical and chemical state of the interstellar medium (ISM). Early work quantifying the cosmic optical and infrared backgrounds (COB and CIB, respectively) found that half of starlight is reprocessed by dust into the infrared (e.g., Lagache et al. 2005; Dole et al. 2006), highlighting the importance of combining direct and indirect tracers to measure the total SFR. Though the COB and CIB are averaged across cosmic time, we now know that dust obscuration peaks along with the general SFR density of the Universe during the epoch of cosmic noon ($1 \lesssim z \lesssim 3$; see Madau & Dickinson 2014, for a review). During this critical era, luminous infrared galaxies¹ dominate the total SFR budget in galaxies, with the obscured star formation component accounting for $\gtrsim 80\%$ of the total SFR in massive galaxies ($\log M_*/M_\odot \gtrsim 10 - 10.5$; Whitaker et al. 2017; Zavala et al. 2021).

Accounting for this obscured SFR component has historically relied on sensitive survey facilities such as Infrared Space Observatory (ISO; Kessler et al. 1996), Spitzer Space Telescope (Werner et al. 2004) and Herschel Space Observatory (Pilbratt et al. 2010), spanning the wide wavelength range and spectral features that encompass the mid- to far-infrared ($\sim 5 - 1000\mu\text{m}$). Studies with these facilities faced two major challenges. First, the poor to moderate spatial resolution at IR wavelengths meant we were confusion limited (Dole et al. 2006), limiting us to relatively shallow sensitivities compared to the UV and optical. Analyses of individual galaxies were limited to the bright end and stacking (Whitaker et al. 2014, 2017) was required to reach galaxies on the main sequence (MS; Elbaz et al. 2011; Popesso et al. 2023), which averaged over galaxy-to-galaxy variations. Pushing past the confusion limit requires larger apertures, such as we now have for the mid-IR with JWST (Gardner et al. 2023; Rigby et al. 2023).

The second challenge is more fundamental. Both the fraction of recent star formation absorbed by dust and the fraction of dust emission coming from young stars vary as a function of galaxy population, cosmic time, and wavelength observed. The relationship between the IR and SFR cannot be easily extrapolated from massive to dwarf galaxies, nor from local to high redshift. For example, in heavily obscured galaxies, the ratio of SFRs derived from the infrared to those derived from hydrogen recombination lines like Pa α at $1.876\mu\text{m}$ increases with increasing infrared luminosity (Alonso-Herrero et al. 2006; Calzetti et al. 2007).

Observing dust in a wide range of populations and redshifts to disentangle these complexities can now be advanced substantially by JWST. In particular, the Mid-Infrared Instru-

ment (MIRI; Rieke et al. 2015; Wright et al. 2023) provides sensitive access to the mid-infrared (observed $\sim 5 - 26\mu\text{m}$) up to $z \sim 3$ through both imaging and spectroscopic modes. In star forming galaxies (SFGs), the mid-IR is dominated by broad emission features from polycyclic aromatic hydrocarbons (PAHs; Smith et al. 2007; Tielens 2008; Li 2020; Lai et al. 2020). The role of PAHs in the ISM is not yet fully known, but it may be substantial: PAHs regulate the chemistry and ionization balance in the ISM (e.g., Tielens & Hollenbach 1985; Bakes & Tielens 1994; Helou et al. 2001) and are tightly correlated with molecular gas (e.g., Pope et al. 2013; Whitcomb et al. 2022; Leroy et al. 2023), which may indicate they act as catalysts for the formation of H₂ molecules (e.g., Bauschlicher 1998; Foley et al. 2018; Barrera et al. 2023).

PAHs are also tightly correlated with star formation on scales from HII regions to entire galaxies (Calzetti et al. 2007). As bright features, PAHs in aggregate typically contribute $\sim 10\%$ of the total infrared emission ($L_{\text{IR}} \equiv L[8 - 1000\mu\text{m}]$ Wu et al. 2010; Shipley et al. 2016) and up to $\sim 20\%$ in extreme cases (Smith et al. 2007). As such, PAHs – along with the rest-frame mid-IR continuum – have a prolific history as a robust measure of the obscured SFR component (Le Flocc’h et al. 2005; Reddy et al. 2006; Elbaz et al. 2011; Magnelli et al. 2011; Wuyts et al. 2011; Whitaker et al. 2012, 2017; Rujopakarn et al. 2013; Shipley et al. 2016; Cluver et al. 2017; Mahajan et al. 2019; Kovács et al. 2019). This has been especially vital at higher redshifts, as previous instruments such as Spitzer/MIPS at $24\mu\text{m}$ (Rieke et al. 2004) directly probed the rest-frame $8\mu\text{m}$ spectral region during cosmic noon.

The catch, however, is that these studies have largely focused on massive SFGs with roughly solar metallicities, where PAHs are ubiquitous (Elbaz et al. 2005; Yan et al. 2005; Sajina et al. 2007) and relatively well behaved. In these galaxies, stellar energy is largely absorbed and re-radiated by dust, such that the total infrared luminosity is closely representative of the bolometric luminosity of young stars, making it an excellent proxy not only for the obscured SFR but also the total SFR (Kennicutt & Evans 2012). On the other hand, in the most heavily obscured SFGs, the ratio of the SFR derived from the IR to that derived from e.g. Pa α is known to increase with increasing L_{IR} . This trend might arise because in these environments the dust competes for a fraction of the ionizing photons (Alonso-Herrero et al. 2006). Or alternatively, that the dust is hotter, increasing the IR output relative to the true SFR (Calzetti et al. 2007). This discrepancy has not yet been solved and needs to be considered when evaluating IR- (and optical-)based SFRs.

With MIRI, we can now go beyond the most massive galaxies, to more fully understand the mid-IR spectrum and its utility as an indirect SFR tracer in main sequence galaxies (e.g., Kirkpatrick et al. 2023; Ronayne et al. 2023) during cosmic noon. A fresh calibration is necessary: in this regime, we expect galaxies to be progressively less metal-rich (Maiolino & Mannucci 2019), with lower dust masses and evolving dust properties as conditions change in the ISM

¹ Commonly termed LIRGs ($10^{11} < L_{\text{IR}}/L_\odot < 10^{12}$) and ultra-LIRGs or ULIRGs ($10^{12} < L_{\text{IR}}/L_\odot < 10^{13}$).

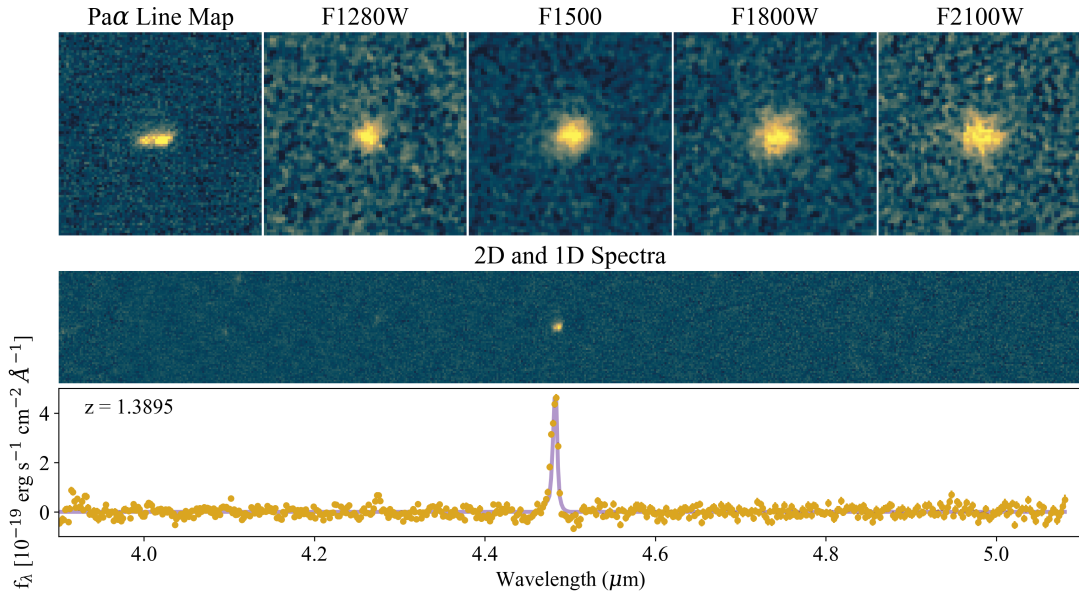


Figure 1. An example of a $\text{Pa}\alpha$ emitter at $z = 1.3895$. The top row shows image cutouts of the $\text{Pa}\alpha$ line map and the F1280W, F1500W, F1800W, and F2100W bands, which contain PAH features at this redshift. The middle and bottom rows show the NIRCcam grism F444W 2D and 1D spectra, respectively. The best fit is shown via the purple line.

(e.g., Rémy-Ruyer et al. 2015; Chastenet et al. 2025). PAHs in particular are known to be sensitive to metallicity and the local radiation field, with lower metallicity galaxies having lower PAH abundances both locally (Engelbracht et al. 2005; Madden et al. 2006; Draine & Li 2007; Marble et al. 2010; Rémy-Ruyer et al. 2015; Aniano et al. 2020; Chastenet et al. 2025) and at cosmic noon (Shivaei et al. 2024).

At the same time, the global dust properties are also changing: the obscured fraction of star formation, driven moreso by far-IR emitting, large grains in thermal equilibrium, is strongly correlated with stellar mass (e.g., Whitaker et al. 2017). This leads to the unobscured SFR component becoming substantial. Finally, IR emission is also known to arise from stellar populations with a range of ages, such that in local, low SFR regions and galaxies, up to $\sim 30 - 80\%$ of the emission at $\sim 8\mu\text{m}$ can come from evolved stars *not* associated with recent star formation. This contribution decreases with increasing SFR and is considered negligible in SFGs at cosmic noon as the MS evolves to higher typical SFRs. However, it is a critical point in more quiescent populations (Leja et al. 2019b; Hayward et al. 2014; Fumagalli et al. 2014).

Given all of these factors, the mid-infrared contains substantial information about the conditions of the ISM and recent star formation. In this work, we examine the behavior of the mid-IR spectrum as a SFR proxy, primarily the rest-frame $8\mu\text{m}$ regions dominated by the luminous $7.7\mu\text{m}$ PAH, which contributes up to 50% of the total PAH emission and $\sim 70\%$ of the emission at $\sim 8\mu\text{m}$ (Smith et al. 2007). We calibrate this behavior against a fiducial SFR indicator; namely, we take advantage of JWST’s access to the $\text{Pa}\alpha$ emission line, a near-infrared hydrogen recombination line previously established as a “gold standard” SFR indicator in local studies (e.g. Alonso-Herrero et al. 2006; Calzetti et al. 2007). $\text{Pa}\alpha$

directly probes the ionizing photons from very young stars (with timescales $\lesssim 10$ Myr; e.g., Leitherer 1990; Rigby & Rieke 2004) and is relatively insensitive to dust attenuation compared to the more commonly-used Balmer emission lines (Rieke et al. 2009; Cleri et al. 2022; Giménez-Arteaga et al. 2022; Reddy et al. 2023b; Neufeld et al. 2024; Calzetti et al. 2025), which can fail to account for optical thick star formation (Reddy et al. 2026). A combination of MIRI imaging and NIRCcam grism spectroscopy via the SMILES and FRESCO surveys is used to build a sample of MS SFGs, free of the selection bias of previous analyses using targeted spectroscopy. With this, we formulate MIRI-based and composite UV+IR SFR calibrations down to MS galaxies with $\log M_*/M_\odot \sim 9$ and SFRs ~ 1 and assess their quality and applicability over the redshift range $0.3 < z < 3$.

As the area of these surveys limits the number of luminous galaxies in our main calibration sample, we also examine the use of SFR indicators at the bright end using data from the literature and a small sample of local ULIRGs with JWST/NIRSpec (Jakobsen et al. 2022; Böker et al. 2023) spectroscopy (Perna et al. 2024; Rieke et al. 2025). Specifically, we address two issues: 1) whether the PAH deficits at high L_{IR} observed in local galaxies apply to IR-based SFRs at higher redshift. And 2) we use multiple hydrogen recombination lines detected in the local ULIRG sample to measure accurate extinction-corrected $\text{Pa}\alpha$ SFRs in very luminous sources. We compare this to IR-based SFRs, addressing whether $\text{Pa}\alpha$ can give accurate SFR determinations in these extreme galaxies, or whether infrared approaches are preferred.

This paper is organized as follows: in Sections 2 we present the datasets used in this study and in 3 we describe the selection of our $\text{Pa}\alpha$ emitter sample and SED fitting.

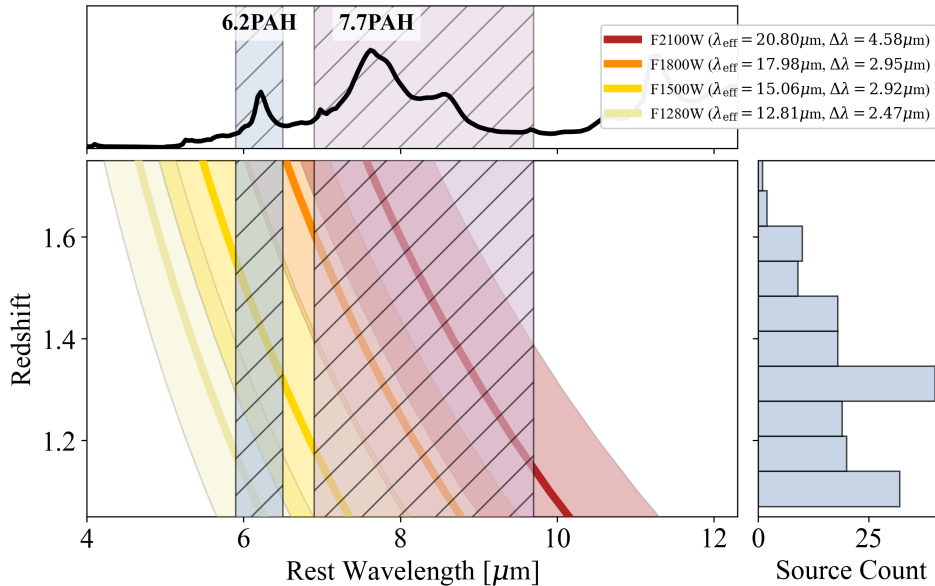


Figure 2. The rest wavelengths and bandwidths of four MIRI filters (F1280W, F1500W, F1800W, F2100W) over the redshift range $1 < z < 1.75$. The F1800W and F2100W filters are dominated by the $7.7 \mu\text{m}$ PAH emission complex (top panel). The narrower $6.2 \mu\text{m}$ PAH emission line (top panel) falls mostly in the F1500W, with partial coverage in the F1280W. The width of the PAHs features (Draine et al. 2021) is shown via the hatched regions. (top) The mid-infrared regions of a representative $\log L_{\text{IR}}/L_{\odot} = 11.25$ SFG template from Rieke et al. (2009). (right) A histogram of the redshifts of the sources used in this study.

In Section 4, we derive our fiducial SFRs from the $\text{Pa}\alpha$ emission line corrected for attenuation via both hydrogen recombination line ratios and SED fitting. Our main analysis is presented in Section 5, which uses the fiducial $\text{Pa}\alpha$ SFRs to examine the behavior of the rest-frame $8 \mu\text{m}$ spectral region via MIRI photometry and calibrate SFR indicators via monochromatic flux densities, total infrared luminosities, and composite UV+IR relations. Section 6 discusses the general robustness and applicability of our calibrations, including causes of scatter and outliers. Finally, in Section 7, we examine SFR estimation for very luminous infrared galaxies. Our conclusions are presented in Section 8. In this work, we use the standard flat ΛCDM cosmology from (Planck Collaboration et al. 2020). Any magnitudes quoted are AB mag (Oke & Gunn 1983). Scatter is quoted using the normalized median absolute deviation (NMAD), $\sigma_{\text{NMAD}} \approx 1.4826 \times \text{MAD}$.

2. DATA

2.1. SMILES MIRI: Data Reduction and Photometric Extraction

The Systematic Mid-infrared Instrument Legacy Extragalactic Survey (SMILES; Rieke et al. 2024; Alberts et al. 2024) imaged $\sim 34 \text{ arcmin}^2$ of the GOODS-S field in 8 MIRI imaging filters. This work focuses primarily on the four mosaics at $\sim 12 - 21 \mu\text{m}$, F1280W, F1500W, F1800W, and F2100W, which reached 5σ point source sensitivities of

$0.62, 0.75, 1.8,$ and $2.8 \mu\text{Jy}$, respectively². We use aperture photometry based on Kron (Kron 1980) apertures, with photometric uncertainties determined by placing random apertures across the source-masked image. For a full description of the data reduction and photometric catalog, see Alberts et al. (2024).

2.2. FRESCO: Spectral Extraction and Line Properties

The First Reionization Epoch Spectroscopically Complete Observations survey (FRESCO; Oesch et al. 2023) obtained NIRCcam wide field slitless spectroscopy (WFSS) and associated direct imaging in GOODS-N and GOODS-S, with the latter overlapping the SMILES MIRI imaging described in Section 2.1. Spectra were obtained using grismR in a single dispersion direction with the F444W filter, providing continuous wavelength coverage over $\sim 3.8 - 5 \mu\text{m}$. Direct imaging was obtained in the F182M, F210M, and F444W filters to 5σ depths of 28.4, 28.2, and 28.2 mag, respectively. The FRESCO data reduction was performed using grizli (Brammer & Matharu 2021) and will be presented in G. Brammer et al. (in prep). Source extraction is based on a stacked detection image, created from the FRESCO direct imaging.

With 7 ks exposure times per pointing with the grism, FRESCO reaches a 5σ line sensitivity of $2 \times 10^{-18} \text{ ergs s}^{-1} \text{ cm}^{-2}$ with $R \sim 1600$. As slitless spectroscopy, this provides a complete, flux-limited census of line emitters, free of

² We note that we do not use the F2550W imaging from SMILES due to its poorer sensitivity limit of $17 \mu\text{Jy}$ (5σ ; Alberts et al. 2024).

the selection effects associated with slit spectroscopy. In this work, we focus on the Pa α line, which falls in the F444W filter at $1 < z < 1.75$. In Figure 1, we show NIRC*am* and MIRI cutouts and the 2- and 1D spectra for an example Pa α emitter in the SMILES field.

2.3. Other Data

NIRC*am* kron photometry is adopted from the JWST Advanced Deep Extragalactic Survey (JADES; Eisenstein et al. 2026; Rieke & the JADES Collaboration 2023) DR1 release which includes the following: 1) HST ACS photometry covering 0.4–0.85 μ m with 5 filters from the Hubble Legacy Field (Illingworth et al. 2016; Whitaker et al. 2019), NIRC*am* 0.9–4.4 μ m photometry in 6 filters from JADES and NIRC*am* medium band coverage (F182M, F210M, F430M, F460, F480M) from the JWST Extragalactic Medium-band Survey (JEMS; Williams et al. 2023). The NIRC*am* data reduction and photometry catalogs are described in Rieke & the JADES Collaboration (2023). The 5 σ point source sensitivities reached are on order 2–22 nJy (28.3–30 mag).

The GOODS-S field contains extensive spectroscopic coverage, mostly from targeted campaigns. For verification of a subset of the FRESCO grism-based redshifts, we use spectroscopic redshifts from JADES NIRSpec (Bunker et al. 2024; D’Eugenio et al. 2025), MUSE (Urrutia et al. 2019; Bacon et al. 2023), ASPECS (Walter et al. 2016), and compilations of various sources in the literature for the CANDELS fields (Kodra et al. 2023). Finally, H α + $[\text{NII}]$ emission line fluxes are obtained from the publicly available CANDELS Ly α Emission at Reionization (CLEAR) catalog from Simons et al. (2023), which were derived based on HST G102 and G141 grism spectroscopy. At the HST grism resolution ($R \sim 100 - 200$) H α is blended with $[\text{NII}]$ and so we extract the H α line fluxes from the blended catalog fluxes by adopting the $[\text{NII}]/\text{H}\alpha$ line ratio - stellar mass relation at $z \sim 2$ from Sanders et al. (2021). The line ratio ranges from 0.06 – 0.23 over $\log M_*/M_\odot \sim 9 - 10.6$ and we deblend the lines as follows:

$$f_{\text{H}\alpha} = f_{\text{H}\alpha+[\text{NII}]} \times \frac{1}{1 + [\text{NII}]/\text{H}\alpha} \quad (1)$$

We note the ratios have been corrected for the contribution from diffuse ionized gas to the line emission (Sanders et al. 2017; Zhang et al. 2017; Sanders et al. 2021) and that we don’t account for any dependence of the ratio on SFR (as motivated by e.g., Wuyts et al. 2016).

3. SAMPLE AND SED FITTING

3.1. Sample Selection

To build our sample, we start with the 271 Pa α emitters with a $> 4\sigma$ line detection that are within the SMILES footprint. We match this catalog to the SMILES MIRI and JADES NIRC*am* detection catalogs with a search radius of 0.3”, finding 194 matches. We then perform an inspection and further remove 15 matches based on their NIRC*am* grism spectra (i.e. visual inspection reveals the Pa α

line is not at the redshift of existing spec-*zs* or we identify double-peaked lines that may not yield a robust Pa α flux) and an additional 10 which are blended or near the mosaic edge in MIRI. This leaves a robust sample of 169 Pa α emitters with MIRI+NIRC*am* photometric counterparts. The redshift distribution of this parent sample, spanning $z \sim 1 - 1.7$ as set by the F444W grism filter, is shown in Figure 2 compared with the central (rest) wavelength of the F1280W, F1500W, F1800W, and F2100W filters over this range. The width of each filter is indicated by the shaded bands. The hatched regions show the width of the 6.2 μ m and 7.7 μ m PAH complexes, as defined in Draine et al. (2021). The 6.2 μ m PAH enters the F1280W, F1500W, F1800W and F2100W filters at $z \sim [0.8, 1.1, 1.55, 1.85]$ and exits at $z \sim [1.38, 1.8, 2.3, 2.9]$, respectively. For the 7.7 μ m PAH, the z bounds are $z \sim [0.2, 0.4, 0.7, 0.9]$ and $z \sim [1, 1.37, 1.79, 2.3]$.

Given the strength and width of the 7.7 μ m PAH feature, our focus will be on the F1800W and F2100W fluxes of our sample. The SMILES catalog provides forced photometry in all bands 10 μ m and longer, regardless of SNR, based on a F560W+F770W detection image (see Section 2). From our parent sample of 169, 128 (79%) have a $\geq 3\sigma$ detection in either F1800W or F2100W; 48 (28%) have $1 - 3\sigma$ photometric measurements in F1800W and/or F2100W; and 15 (8%) are completely undetected with $< 1\sigma$ forced photometry. The marginally detected and undetected sub-samples will be incorporated using stacking.

In addition, we visually examine the 77 Pa α sources with no MIRI counterpart, finding that 34/77 are blended with a neighbor and the remaining 44 are low mass (median $\log M_*/M_\odot \sim 8.5$), below the approximate mass completeness limit estimated in Shivaei et al. (2024). These Pa α emitters with no MIRI counterpart are combined with the 15 emitters with $< 1\sigma$ in F1800W and F2100W and will be incorporated into the main analysis by stacking their MIRI cutouts.

Finally, to identify AGN, we match these to the catalogs from Lyu et al. (2022) and Lyu et al. (2024); 18 have evidence for AGN from the X-ray and/or mid-infrared. These sources will be excluded from the main analysis but are discussed in Section 6.2.4.

3.2. SED Fitting

SED fitting is done with full HST, NIRC*am*, and MIRI photometry using the Bayesian fitting code *Prospector* (Leja et al. 2019a; Johnson et al. 2021) and the Flexible Stellar Population Synthesis (FSPS) code (Conroy et al. 2009; Conroy & Gunn 2010). We direct the reader to Ji et al. (2023) for a detailed description of our *Prospector* setup, which we summarize here. The star formation history (SFH) assumed is non-parametric with the continuity prior (Leja et al. 2019a) and is composed of 9 lookback time bins, where the SFR is constant in each bin³. The first two time bins are fixed

³ As shown in Leja et al. (2019a) using simulated galaxy catalogs, the best-fit properties are insensitive to the number of bins used above five bins.

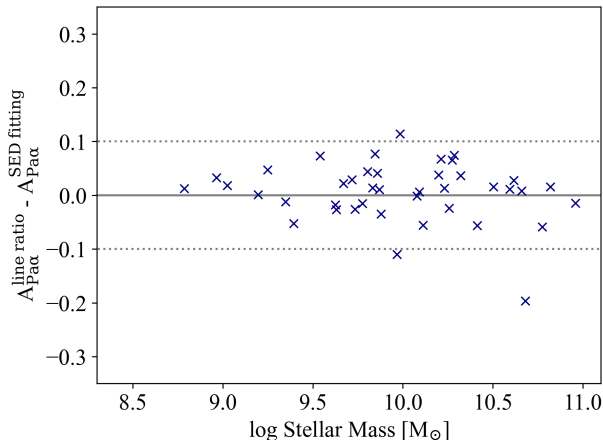


Figure 3. The difference in $A_{\text{Pa}\alpha}$ derived from the $\text{Pa}\alpha/\text{H}\alpha$ line ratio and from SED fitting as a function of stellar mass. The two measurements are in good agreement within 0.1 mag (dotted lines), corresponding to a difference in the final $\text{Pa}\alpha$ flux of $\lesssim 10\%$.

to be 0 – 30 and 30 – 100 Myr to capture recent star formation activity with a relatively high time resolution. SED fitting with a nonparametric SFH using `Prospector` produces high quality reconstructions of the SEDs and SFHs of synthetic galaxies in cosmological simulations, with low systematic biases (Leja et al. 2019a; Johnson et al. 2021; Tacchella et al. 2022; Ji et al. 2023).

Nebular continuum and line emission modeling is based on Byler et al. (2017). For dust attenuation, we assume a two-component model (Tacchella et al. 2022) where the attenuation of nebular emission and young populations is treated differently from that of old stellar populations (Charlot & Fall 2000). Stellar populations older than 10 Myr are parameterized using a modified Calzetti Law (via a variable slope; Noll et al. 2009) with the UV dust bump at 2175 Å tied to the slope of the attenuation following Kriek & Conroy (2013). The attenuation of the young population is assumed to be an inverse function of wavelength and tied to the attenuation of the old population via a clipped normal prior on their ratio, centered at 1, with a width of 0.3 and a range of 0 – 2 (Ji et al. 2023). We allow the stellar and gas-phase metallicity as well as the ionization parameter U to vary. We additionally allow an AGN component and check that the addition of this component does not significantly alter our fits. From our fits, we obtain stellar masses, SED-fitted SFRs, mass-weighted ages, and a dust attenuation models.

4. FIDUCIAL STAR FORMATION RATES FROM $\text{Pa}\alpha$

For our goal of calibrating SFRs using MIRI imaging, we obtain fiducial SFRs from the $\text{Pa}\alpha$ emission line. Compared to the commonly used stronger Balmer lines, the Paschen lines emit in the near-infrared and therefore are less susceptible to dust extinction; in extreme examples of dusty regions in local SFGs with $A_V \sim 10 - 30$, $A_{\text{Pa}\alpha}$ is found to be < 2 mag and optically thin (Murphy et al. 2001; Dannerbauer et al. 2005; Armus et al. 2007). With JWST, we are just now

starting to expand the use of $\text{Pa}\alpha$ to higher redshifts; recent works with NIRSpec and NIRCam found higher SFRs implied by $\text{Pa}\alpha$ as compared to $\text{H}\alpha$ and spatial offsets in their emission that may indicate optically thick star formation is being missed by $\text{H}\alpha$ in MS galaxies at cosmic noon (Reddy et al. 2023a, 2025; Lorenz et al. 2025).

To determine the attenuation of $\text{Pa}\alpha$ in our sample and obtain total SFRs, we first derive $A_{\text{Pa}\alpha}$ using the ratio of $\text{Pa}\alpha$ to $\text{H}\alpha$ for sources where $\text{H}\alpha$ is available from CLEAR (Section 2.3). As intrinsic hydrogen recombination line ratios can be predicted given reasonable assumptions on electron density and temperature (Osterbrock 1989), they are often used as a direct measure of nebular line attenuation. From the CLEAR catalog, we find 56 matches to our sample with $\text{H}\alpha$ + [NII] fluxes detected at greater than 5σ and no evidence for AGN activity. We remove the [NII] contribution as described in Section 2.3. The nebular extinction is then

$$E(B - V)_{\text{neb}} = \frac{2.5}{\kappa_{\text{H}\alpha} - \kappa_{\text{Pa}\alpha}} \times \frac{\log(f_{\text{Pa}\alpha}/f_{\text{H}\alpha})}{0.109} \quad (2)$$

where 0.109 is the intrinsic (dust-free) line ratio under Case B recombination (Hummer & Storey 1987; Reddy et al. 2023b). We adopt the Galactic extinction curve from Cardelli et al. (1989) with $R_V = 3.1$, which has been shown to well approximate the nebular attenuation curve in the optical at $z \sim 2$ (Reddy et al. 2015, 2020). We find 13 measurements of $A_{\text{Pa}\alpha}$ that are negative, likely indicating uncertainty in removing [NII] from $\text{H}\alpha$. Of the remainder, the median $A_{\text{Pa}\alpha}$ from the $\text{Pa}\alpha/\text{H}\alpha$ line ratio is 0.06 mag with a scatter of $\sigma_{\text{NMAD}} = 0.06$.

For the portion of our sample without an $\text{H}\alpha$ match or a negative $A_{\text{Pa}\alpha}$ derived from the $\text{Pa}\alpha$ to $\text{H}\alpha$ ratio⁴, we derive the correction from our SED fitting with `Prospector`. The description of the two-component dust attenuation model is described in Section 3.2. As our fits were done with photometry only, we assume that the attenuation curve of the older stellar population (> 10 Myr) is more robustly constrained, which gives us the stellar attenuation. To obtain $A_{\text{Pa}\alpha}$ we then assume that the stellar and nebular attenuation are equal. We show that this results in good agreement between the $A_{\text{Pa}\alpha}$ derived from the $\text{Pa}\alpha$ - $\text{H}\alpha$ line ratios vs the SED fitting in Figure 3 for the sub-sample where we can measure both. Our assumption is likely appropriate for our high mass $\text{Pa}\alpha$ emitters (Reddy et al. 2020; Shivaei et al. 2020). For dwarf galaxies at $z \sim 2$, the relationship between nebular and stellar reddening is found to be closer to that originally derived for local starbursts (~ 2 ; Calzetti et al. 2000; Reddy et al. 2020; Shivaei et al. 2020); however, this relationship is also known to have significant scatter and as the attenuation of $\text{Pa}\alpha$ is predicted to be especially low in dwarf galaxies, we expect our assumption to have negligible impact on our results.

⁴ The majority of the sources with negative $A_{\text{Pa}\alpha}$ are $\log M_*/M_\odot < 9.5$ and have attenuation consistent with zero from the SED fitting.

Our final $A_{\text{Pa}\alpha}$ values are shown as a function of the A_V derived from SED fitting in Figure 4. We display the relation expected for a Calzetti attenuation curve ($A_V/A_{\text{Pa}\alpha} = 6$) for reference (Calzetti et al. 2007). We correct the Pa α line luminosities as

$$L_{\text{Pa}\alpha, \text{corr}} = L_{\text{Pa}\alpha} 10^{0.4A_{\text{Pa}\alpha}} \quad (3)$$

Overall, we find $A_{\text{Pa}\alpha}$ is largely < 0.2 mag, corresponding to a less than 20% correction for dust attenuation, in good agreement with previous studies (Reddy et al. 2018, 2023a; Neufeld et al. 2024).

From the attenuation corrected Pa α luminosities, we then calculate our fiducial SFR $_{\text{Pa}\alpha}$ using the calibration presented in Reddy et al. (2023b) as

$$\text{SFR}_{\text{Pa}\alpha}^{\text{R23}} [M_{\odot} \text{ yr}^{-1}] = C(\text{Pa}\alpha) L_{\text{Pa}\alpha, \text{corr}} [\text{ergs s}^{-1}] \quad (4)$$

where $C(\text{Pa}\alpha) = 1.95 \times 10^{-41}$ and 3.9×10^{-41} for sub-solar ($Z_{\star} = 0.001$) and solar ($Z_{\star} = 0.02$ or $12 + \log(\text{O}/\text{H}) = 8.69$) metallicities, respectively. This calibration takes into account 1) that the ionizing photon rate increases with decreasing metallicity at fixed SFR (Chisholm et al. 2019) and 2) that stellar binarity has been shown as important in optical line calibrations (Steidel et al. 2016; Reddy et al. 2022). As in Reddy et al. (2023a), the solar metallicity calibration is adopted for all galaxies at $z \leq 1.4$ and for high mass galaxies ($\log M_{\star}/M_{\odot} > 10.45$) at $z \geq 1.4$. Sub-solar metallicity is adopted for low-mass galaxies at $z \geq 1.4$. This Pa α SFR calibration will be adopted throughout the paper. As a check, we will also verify all of our results using a non-metallicity

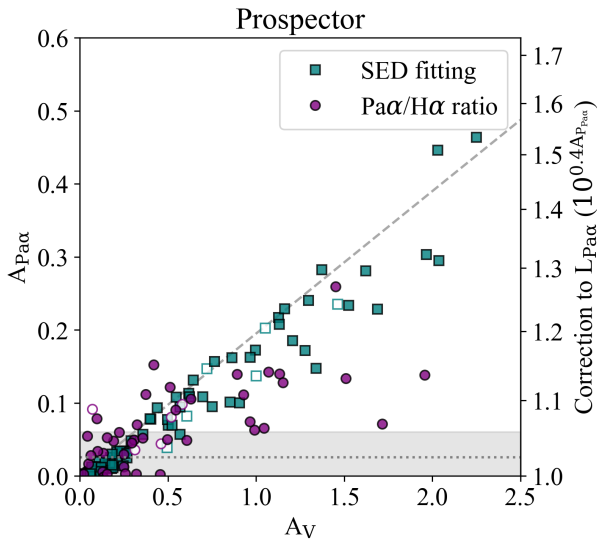


Figure 4. $A_{\text{Pa}\alpha}$ and the correction factor $10^{0.4A_{\text{Pa}\alpha}}$ (right axis) as a function of A_V for values derived from SED fitting (blue squares) and from the Pa α /H α line ratios (purple circles). Open symbols denote AGN. The dotted line and shaded region show the median value 0.03 with a scatter of 0.04 dex. The dashed line shows the relation $A_V/A_{\text{Pa}\alpha} = 6$ (Calzetti et al. 2007).

dependent calibration as in Shipley et al. (2016): $\log \text{SFR} [M_{\odot} \text{ yr}^{-1}] = -40.33 + \log L_{\text{Pa}\alpha} [\text{ergs s}^{-1}]$.

The final Pa α based fiducial SFRs, spanning a range of $\sim 0.5 - 40 M_{\odot} \text{ yr}^{-1}$, are shown as a function of stellar mass in Figure 5. We sample the full range of the MS ($-0.3 < \Delta \text{MS} < 0.3$) over the range $\log M_{\star}/M_{\odot} \sim 9 - 10.8$ and reach over an order of magnitude lower in SFR than the MIPS24 confusion limit (Dole et al. 2004) at $z \sim 1.3$.

5. CALIBRATION OF MID-INFRARED-BASED SFR INDICATORS WITH MIRI

In this section, we derive a SFR calibration for the MIRI broadband photometry using our fiducial Pa α SFRs. In the redshift range of our sample ($1 \lesssim z \lesssim 1.75$), the MIRI broadband filters at $12 - 21 \mu\text{m}$ contain PAH emission as well as small grain dust and stellar continuum emission. The F1800W and F2100W bands are dominated by the strong $7.7 \mu\text{m}$ PAH over the full redshift range and the F1280W and F1500W filters contain the narrower $6.2 \mu\text{m}$ PAH at $z \lesssim 1.3$ and $1.2 \lesssim z \lesssim 1.6$, respectively (Figure 2). To use the cleanest calibration sample possible, we remove 1) 18 AGN, which may influence PAHs (e.g., Diamond-Stanic & Rieke 2010; Inami et al. 2018; García-Bernete et al. 2022; Lai et al. 2022) and Pa α ; 2) 18 non-AGN starbursts ($\Delta \text{MS} > 0.6$; e.g., Rodighiero et al. 2011), where intense radiation fields may influence the PAHs (e.g., Kim et al. 2024); and 3) 6 Pa α emitters below the MS ($\Delta \text{MS} < -0.6$), where dust heating may not be related to young stars (e.g., Hayward et al. 2014). Our clean calibration sample contains 126 Pa α emitters. The removed outliers will be examined related to the clean sample and calibration in Section 6.2.

5.1. The relationship between Pa α and the $8 \mu\text{m}$ mid-infrared spectral region

In Figure 6, we show the luminosity of the rest-frame $8 \mu\text{m}$ spectral region as measured by MIRI longwave filters as a function of the extinction-corrected Pa α line luminosity (panel a) and SFR $_{\text{Pa}\alpha}$ (panel b). To sample the same spectral features as much as possible across our redshift range, we adopt the observed F1800W luminosity for the lower half of our redshift range and F2100W for the upper half such that

$$L_{8\mu\text{m}, \text{rest}} = \begin{cases} L_{\text{F1800W}} & \text{for } z < 1.4 \\ L_{\text{F2100W}} & \text{for } z \geq 1.4 \end{cases} \quad (5)$$

where $L_x \equiv \nu L_{\nu}$. We make no correction for the different filter transmission curves nor do we apply a k-correction here (see Section 5.3).

For Pa α sources with marginal or no detection at F1800W or F2100W, we perform inverse-variance weighted and median stacking with bootstrapping in two categories: 1) clean

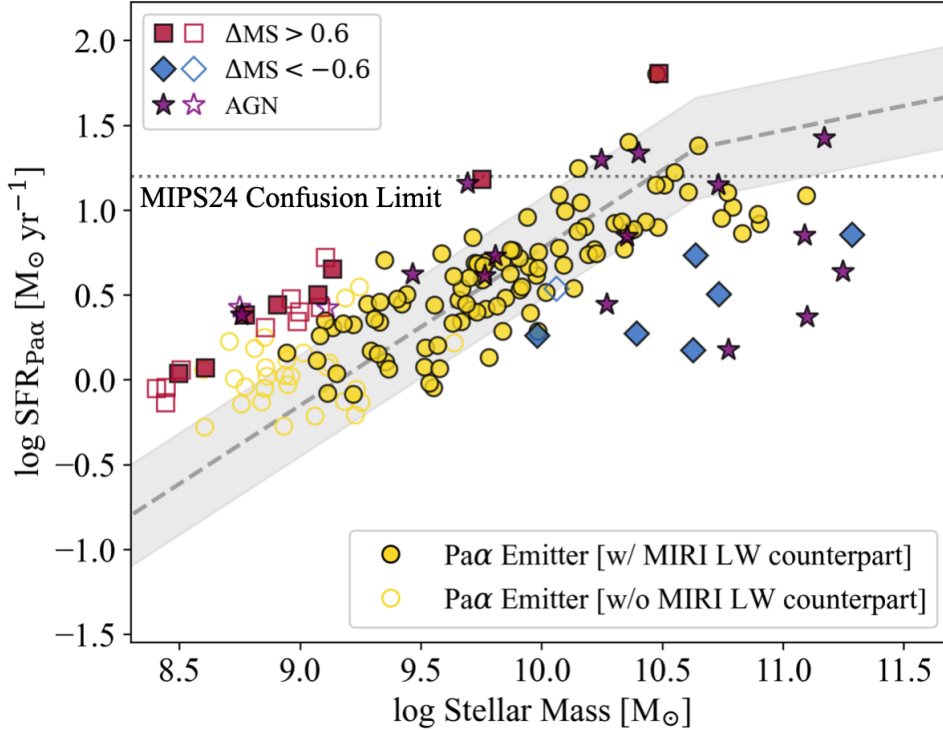


Figure 5. SFR versus stellar mass for the Pa α emitters in our sample. Solid (open) circles show Pa α emitters on the MS detected (undetected) in MIRI long wavelength filters (F1800W or F2100W). The dashed line and shaded region shows the MS at $z \sim 1.3$, the median redshift in our sample. Pa α emitters above the MS ($\Delta\text{MS} > 0.6$), below the MS ($\Delta\text{MS} < -0.6$), and hosting AGN are shown as red squares, blue diamonds, and purple stars, respectively. The MIPS 24 μm confusion limit at $z \sim 1.3$ is shown as a dotted line.

samples⁵ with a marginal $\text{SNR} = 1 - 3$ measurement in F1800W or F2100W and 2) a clean sample with $\text{SNR} < 1$ in both red filters or no MIRI counterpart based on the F560W+F770W detection image (see Section 2.1). For the former, the stacks of 17 and 13 marginally detected sources in F1800W and F2100W, respectively, are detected at $\sim 4 - 5\sigma$, while splitting this sample by redshift (Eqn 5) yields stacks⁶ detected at $\sim 6 - 7\sigma$. We verify that the weighted average stacks are consistent with median stacks, ruling out a bias toward outliers. These stacks will be used in the calibration of the MIRI SFRs. The second, undetected sample (29 sources) is not detected via stacking in either filter and has significant differences between the weighted and median stack, indicating this subsample contains outliers. From the median stacks and bootstrapped errors we derive 3σ upper limits, which we will check against our calibration for consistency.

In Figure 6 (left) we show $L_{8\mu\text{m},\text{rest}}$ versus $L_{\text{Pa}\alpha}$ in log space. To quantify the behavior of $L_{8\mu\text{m},\text{rest}}$, we perform fitting using orthogonal distance regression (ODR) from the `scipy` software package (Virtanen et al. 2020), which takes

into account uncertainties in both parameters⁷. Fitting is done to Pa α emitters with F1800W or F2100W $\text{SNR} \geq 3$ and to the stacks of those with $\text{SNR} = 1 - 3$. We start with a single component linear fit, finding a superlinear slope with $\alpha = 1.9 \pm 0.1$ with a scatter of 0.38 dex. This is somewhat steeper than the slope derived in Ronayne et al. (2023), which used the dust-corrected UV as their fiducial SFR indicator. We note, however, their use of SED fitting to isolate $L_{7.7\text{PAH}}$ differs from our approach of using the total broadband fluxes, which contain PAH plus continuum emission.

As discussed in the introduction, however, pre-JWST studies have firmly established that for massive, high SFR galaxies, there is a unity relation between the mid- and far-IR and SFR (Rujopakarn et al. 2013; Shipley et al. 2016; Alonso-Herrero et al. 2006; Papovich et al. 2007; Wuyts et al. 2011; Pope et al. 2008; Siana et al. 2008, 2009; Rieke et al. 2009; Zhu et al. 2008), such that we expect our superlinear fit to turn over at some threshold. This is visually demonstrated in Figure 6 by two lensed galaxies at $z \sim 2.5$ in which both Pa α and the 7.7 μm PAH were detected by Spitzer/IRS (Rujopakarn et al. 2011; Shipley et al. 2016). Given 1) the small areal coverage of SMILES relative to pre-JWST MIR surveys and 2) the typical SFRs of the MS galaxies in the redshift

⁵ Meaning AGN, starbursts, and sources significantly below the MS have been removed.

⁶ To create a combined stack, we first split by redshift at $z = 1.4$ (Eqn 5) and stack separately in F1800W and F2100W and then combine the stacked fluxes weighted by the number in each stack

⁷ As only measurement uncertainties are used in the fits, we impose a ceiling of $\text{SNR} = 20$, equivalent to assuming $\sim 5\%$ systematic uncertainty, to keep very luminous sources from driving the fit.

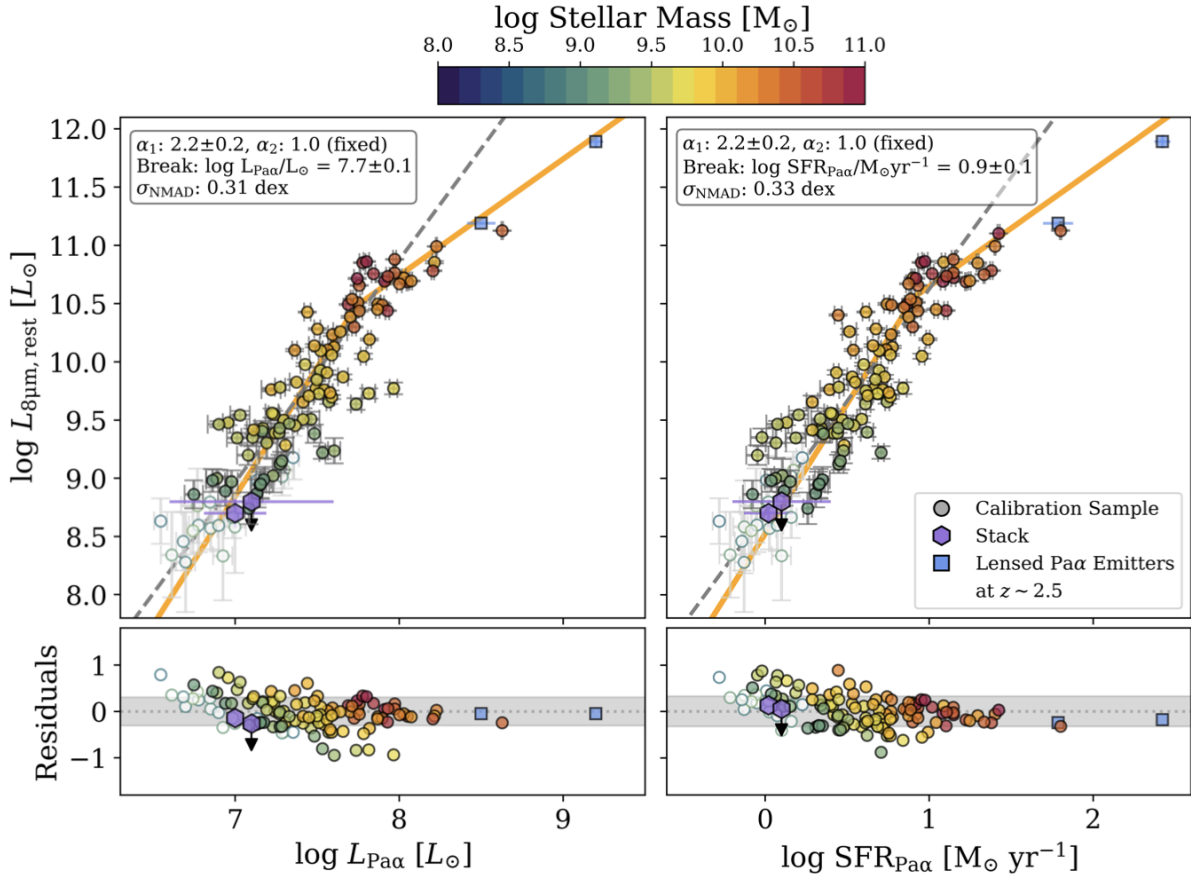


Figure 6. (left) The relation between the extinction-corrected Pa α luminosity and the observed $L_{8\mu\text{m, rest}}$ (Eqn 5) for MS galaxies with (closed circles) and without (open circles) a $> 3\sigma$ detection in F1800W or F2100W. The purple hexagons show the stack of the Pa α emitters with only marginal detections ($\text{SNR} = 1 - 3$) in F1800W or F2100W and the upper limit on the stack of Pa α emitters with no MIRI detection. The blue squares show two lensed galaxies with measurements of Pa α and the $7.7\mu\text{m}$ PAH feature at $z \sim 2.5$ (Rigby et al. 2008; Rujopakarn et al. 2011; Shipley et al. 2016). The gray dashed line is a single component linear fit. A broken power law fit (Eqn 6) with free parameters amplitude, breakpoint, and faint end slope is shown via the orange, solid line. The bright end slope is fixed to unity following the literature (e.g., Shipley et al. 2016). The bottom panel shows the residuals from the broken power law fit. (right) The relation between the extinction-corrected Pa α SFR using the Reddy et al. (2023a) calibration and the observed $L_{8\mu\text{m, rest}}$ (Eqn 5). Sample and symbols are as in the lefthand panel. The colorbar corresponds to stellar mass for all panels.

range where we have Pa α (i.e. tens of $M_{\odot} \text{ yr}^{-1}$), we do not expect that our sample will have much overlap with the populations studied in the Spitzer era, but these previous works and the hint of a turn over in our data (Figure 6) motivate us to examine a two component fit.

As such, we fit a broken power law following

$$f(x) = \begin{cases} A \left(\frac{x}{x_{\text{break}}} \right)^{\alpha_1} & \text{for } x < x_{\text{break}} \\ A \left(\frac{x}{x_{\text{break}}} \right)^{\alpha_2} & \text{for } x > x_{\text{break}}. \end{cases} \quad (6)$$

where the amplitude (A), break point (x_{break}), and α_1 are allowed to vary. Following previous studies, we fix $\alpha_2 = 1$. Our two component best-fit has a superlinear slope of $\alpha_1 =$

2.2 ± 0.2 up to $\log L_{\text{Pa}\alpha}/L_{\odot} = 7.7 \pm 0.1$, above which a linear slope fits the turn over in our data. Similarly if we fit $L_{8\mu\text{m, rest}} - \text{SFR}_{\text{Pa}\alpha}$ (Figure 6, [right]), we find the same superlinear slope up to $\text{SFR}_{\text{Pa}\alpha} \sim 8 M_{\odot} \text{ yr}^{-1}$. Our broken power law relation yields a scatter of ~ 0.3 dex, about a factor of 2, comparable with previous studies (e.g., Calzetti et al. 2007; Reddy et al. 2010; Wuyts et al. 2011; Rujopakarn et al. 2013; De Rossi et al. 2018; Ronayne et al. 2023). We confirm that we find a consistent broken power-law fit (with slightly increased scatter) if we instead use the $\text{SFR}_{\text{Pa}\alpha}$ calibration from Shipley et al. (2016), which has no metallicity dependence. We likewise find consistent fits within the uncertainties if we repeat this exercise with L_{F1800W} and L_{F2100W} separately, though we see increased scatter (up to ~ 0.4 dex), likely due to the lack of k -correction (see Section 5.3.1).

Table 1. SFR_{Pαα} – L_x Best-Fit Parameters and Monochromatic L_x -based SFR Calibration

Parameter	SFR _{Pαα} – L_x Fits (Eqn 6)					L_x -based SFR Calibration (Eqn 7)	
	N_{gal}^a	log A	log x_{break}^b	α	σ_{NMAD}	a_x	C_x
$L_{8\mu\text{m,rest}}^c$		10.6	0.9 ± 0.1		0.33		
< x_{break}	74			2.2 ± 0.2		0.45 ± 0.07	3.8 ± 0.2
> x_{break}	21			1.0 (fixed)		–	9.6 ± 0.1
L_{F1800W}		10.5	0.9 ± 0.1		0.35		
< x_{break}	75			2.3 ± 0.3		0.44 ± 0.07	3.7 ± 0.2
> x_{break}	21			1.0 (fixed)		–	9.6 ± 0.1
L_{F2100W}		10.2	0.9 ± 0.1		0.39		
< x_{break}	62			2.4 ± 0.5		0.42 ± 0.1	3.4 ± 0.3
> x_{break}	23			1.0 (fixed)		–	9.3 ± 0.2

NOTE—(a) Number of galaxies with SNR > 3 in a given band. (b) x_{break} is given in $M_{\odot} \text{ yr}^{-1}$. See Section 6.1 for discussion on adopting a redshift-independent break in stellar mass: $\log M_{\star}/M_{\odot} = 10.1$. (c) as defined in Eqn 5.

Table 2. SFR_{Pαα} – L_{IR} Best-Fit Parameters and L_{IR} -based SFR Calibration

Parameter	N_{gal}^a	SFR _{Pαα} – L_{IR} Fits (Eqn 6)				L_{IR} -based SFR Calibration (Eqn 8)	
		log A	log x_{break}^b	α	σ_{NMAD}	a_x	C_x
$L_{\text{IR}}^{\text{F1280W}}$	63	11.3	0.9 ± 0.1		0.21		
< x_{break}				1.9 ± 0.2		0.52 ± 0.01	5.0 ± 0.1
> x_{break}				1.0 (fixed)		–	10.4 ± 0.2
$L_{\text{IR}}^{\text{F1500W}}$	126	11.1	0.9 ± 0.1		0.27		
< x_{break}				2.1 ± 0.2		0.47 ± 0.04	4.4 ± 0.1
> x_{break}				1.0 (fixed)		–	10.4 ± 0.1
$L_{\text{IR}}^{\text{F1800W}}$	122	11.4	0.9 ± 0.1		0.31		
< x_{break}				2.3 ± 0.2		0.44 ± 0.04	4.1 ± 0.1
> x_{break}				1.0 (fixed)		–	10.5 ± 0.1
$L_{\text{IR}}^{\text{F2100W}}$	107	11.4	0.9 ± 0.1		0.31		
< x_{break}				2.2 ± 0.3		0.46 ± 0.06	4.3 ± 0.1
> x_{break}				1.0 (fixed)		–	10.5 ± 0.1

NOTE—(a) Number of galaxies with SNR > 3 in a given band. (b) x_{break} is given in $M_{\odot} \text{ yr}^{-1}$. See Section 6.1 for discussion on adopting a redshift-independent break in stellar mass: $\log M_{\star}/M_{\odot} = 10.1$.

Given that the broken power law provides a good description of the $\text{SFR}_{\text{Pa}\alpha} - L_{8\mu\text{m,rest}}$ relation, we calibrate MIRI-based SFR relations at $z \sim 1.3$ as

$$\log \text{SFR} = \begin{cases} a_x \log L_x - C_x & \text{for } < 8M_{\odot} \text{ yr}^{-1} \\ \log L_x - C_x & \text{for } > 8M_{\odot} \text{ yr}^{-1} \end{cases} \quad (7)$$

where luminosities are in L_{\odot} . As most studies will not have an independent measurement of the SFR, we propose an equivalent breakpoint of $\log M_{\star}/M_{\odot} = 10.1$, based on the MS at $z \sim 1.3$ (Leja et al. 2022); we explore and justify this assumption in Section 6.1.2. Our best-fit parameters are provided in Table 1 for $L_{8\mu\text{m,rest}}$ (Eqn 5), L_{F1800W} , and L_{F2100W} .

5.2. Application to higher redshift

So far we have focused on the rest-frame $8\mu\text{m}$ region as it is well-studied and known to be dominated by the luminous $7.7\mu\text{m}$ PAH in SFGs, contributing $\sim 70\%$ of the flux in the IRAC ch4 band in local galaxies (Smith et al. 2007). Expanding the usefulness of MIRI-based SFRs to $z \gtrsim 2$, however, will need to make use of dust features at shorter wavelengths. We examine here the rest- $6\mu\text{m}$ region, which contains the $6.2\mu\text{m}$ PAH. For F1800W and F2100W, $\gtrsim 70\%$ ⁸ of the $7.7\mu\text{m}$ PAH falls within the band at $0.9 < z < 1.5$ and $1.1 < z < 2.1$, respectively. By comparison, $\gtrsim 70\%$ of the $6.2\mu\text{m}$ PAH falls into F1800W and F2100W at $1.6 < z < 2.2$ and $1.9 < z < 2.85$, respectively. To test whether the rest-frame $6\mu\text{m}$ region is viable as a SFR indicator, we employ the F1280W and F1500W bands over our redshift range. For F1280W, coverage of the dust emission at $6.2\mu\text{m}$ starts at $z \sim 1.3$. The F1500W on the other hand covers dust emission at rest $\sim 6 - 8\mu\text{m}$ over our full redshift range. As in the previous section, we test these bands against the $\text{Pa}\alpha$ luminosities and our fiducial $\text{Pa}\alpha$ SFRs. We find again that our data is well fit with a broken power law with a breakpoint at $\sim 8M_{\odot} \text{ yr}^{-1}$ and similar scatter (~ 0.3 dex), showing the same behavior through the rest $\sim 6\mu\text{m}$ spectral region. This suggests that the $6.2\mu\text{m}$ and $7.7\mu\text{m}$ and their associated underlying continua behave similarly in MS galaxies at $z \sim 1.3$, even in lower mass, lower metallicity galaxies. From this, we conclude that the F1800W and F2100W filters can also be calibrated for the rest $6\mu\text{m}$ region, extending the applicable range up to $z \sim 3$, particularly if we control for the k -correction, as we discuss in the next section. We note that we will not test the viability of the $3\mu\text{m}$ region in this work as the $3.3\mu\text{m}$ PAH is relatively weak and sits on continuum more likely unrelated to young stars. Spectroscopy is therefore needed to characterize this feature beyond the local Universe, see Lyu et al. (2025); McKinney et al. (2025).

5.3. $(UV+)\text{L}_{\text{IR}}$ SFR Calibration using MIRI

⁸ Using the PAH clip points presented in Draine et al. (2021).

In the previous section, we showed that the relation between the observed F1800W or F2100W luminosities from MIRI and our fiducial $\text{Pa}\alpha$ SFRs can be described as a broken power law with a break at $\log M_{\star}/M_{\odot} \sim 10.1$. Though this empirical approach is appealing in that it minimizes assumptions, it has drawbacks. First, it doesn't k -correct to account for redshift, which is particularly important given the large variations as a function of wavelength in the mid-IR spectral region. And, second, for $\log M_{\star}/M_{\odot} \lesssim 10$, we are entering the regime where the obscured component of star formation no longer dominates in cosmic noon galaxies (Whitaker et al. 2017), increasing the uncertainty in extrapolating the obscured SFR to a total SFR. As such, in the next two sections, we refine our MIRI-based SFR calibration by scaling from single-band MIRI photometry to the total dust luminosity $L_{\text{IR}} \equiv L[8 - 1000\mu\text{m}]$ and then accounting for the unobscured SFR component through composite SFR calibration (e.g., Bell et al. 2005; Treyer et al. 2010; Hao et al. 2011; Calzetti et al. 2007; Kennicutt et al. 2007, 2009; Wuyts et al. 2011; Whitaker et al. 2014; Lee et al. 2015; Popesso et al. 2023).

5.3.1. Template-based L_{IR}

The mid-IR spectrum of galaxies undergoes large variations over a short wavelength range due to the broad emission and absorption features (see Figure 2). As such, small variations in the redshift of a source can correspond to large intrinsic photometric scatter for a given mid-IR filter. To remove these variations, standard practices are to k -correct to the same rest wavelength (e.g., Rieke et al. 2009) or quantify the total infrared luminosity from one or more mid- to far-infrared bands using SED fitting and/or by scaling representative templates (e.g., Rujopakarn et al. 2013; Boquien & Salim 2021). This process accounts for the redshift and differences in the shape and width of the filters used.

To derive L_{IR} , we adopt the set of empirical templates from Rieke et al. (2009), which have been shown to represent the SEDs of IR-bright galaxies with a scatter of ~ 0.2 dex in derived IR SFR up to $z \sim 3$ (e.g., Rujopakarn et al. 2013; De Rossi et al. 2018). For simplicity, we first scale a single template with $\log L_{\text{IR}}/L_{\odot} = 11.25$ to the MIRI F1800W and F2100W photometry – separately and accounting for their respective transmission curves – and repeat the calibration against $\text{SFR}_{\text{Pa}\alpha}$ as describe in the previous section. We find that the trends of $L_{\text{IR}}^{\text{F1800W}}$ and $L_{\text{IR}}^{\text{F2100W}}$ with $\text{Pa}\alpha$ can again be described with a broken power law (Eqn 6) with the best-fit α_1 slope and breakpoint (Table 2) consistent with what was found in Section 5.1. This reflects that using a single empirical template is assuming a fixed ratio between L_{MIR} and L_{IR} . However, we find that the scatter is somewhat improved by incorporating the k -correction (reduced by ~ 0.05 dex). Our fits are shown in Figure 7 and we note that our galaxies span the range of $\log L_{\text{IR}}/L_{\odot} \sim 9 - 11.5$ and are mostly in the sub-LIRG regime.

Next we test the full range of Rieke et al. (2009) templates, spanning $\log L_{\text{IR}} \sim 10 - 11.75$. To choose a template for each galaxy, we start with the L_{IR} derived above

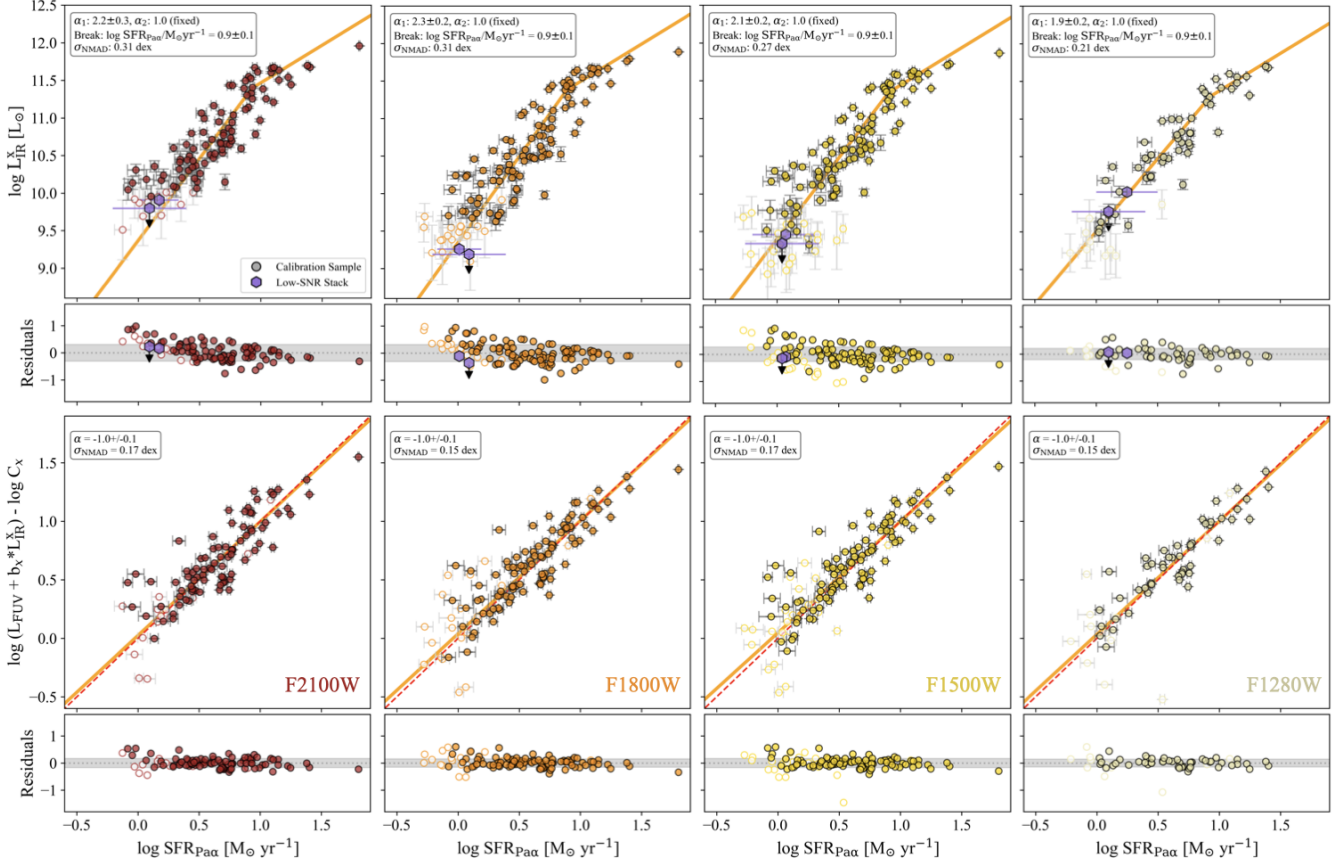


Figure 7. (top panels) L_{IR} derived using single-band MIRI photometry in F2100W, F1800W, F1500W, or F1280W ($z < 1.3$ only) as a function of the fiducial $\text{Pa}\alpha$ SFRs. Symbols and orange, solid line are as in Figure 6. (bottom panels) The UV+IR composite SFR calibration (Eqn 9). The solid orange line is a single component linear fit. The dashed red line is the one-to-one line. The fitted slope and scatter are given in the legend. Closed symbols are detections in both UV and IR, open symbols have $\text{SNR} < 3$ in either.

and then iterate until convergence to adopt the template closest to the galaxy’s actual L_{IR} . We find, however, that this *increases* the scatter when we then compare to $\text{SFR}_{\text{Pa}\alpha}$. This is not wholly unexpected. Studies of highly star-forming ($> 100 M_{\odot} \text{ yr}^{-1}$) galaxies at cosmic noon found that the L_{IR} derived using MIPS $24\mu\text{m}$ agreed better with the L_{IR} measured with longer Spitzer and Herschel bands when using an average template instead of a luminosity-dependent conversion (Papovich et al. 2007; Elbaz et al. 2010; Wuyts et al. 2008; Wuyts et al. 2011). Rujopakarn et al. (2013) likewise showed that the variations in the dust SED correlated with the IR surface density rather than total luminosity. Though MIRI’s spatial resolution will allow the measurement of the IR surface density at cosmic noon for some populations, we want to provide a calibration that does not require this information. Even if we did include it, these studies of massive, IR luminous galaxies may not apply to our sample. UV-selected samples of less massive galaxies, perhaps more analogous to ours, have found significant variation in the ratios of the mid- to far-IR emission (e.g., Reddy et al. 2012; Shivaei et al. 2017; Reddy et al. 2018). As such, we opt to proceed using the single dust template from above to derive L_{IR} for the rest of this work, to minimize scatter. In the next two sections, we

show that the unobscured SFR component is a major source of scatter in our sample and perform a sanity check of the obscured SFR component implied by our choice of template. Then in Section 6, we further discuss the implications of using a single representative IR template in our calibration.

Adopting the $\log L_{\text{IR}}/L_{\odot} = 11.25$ template for the remainder of this study, we calibrate model-dependent MIRI-based SFRs as

$$\log \text{SFR} = \begin{cases} a_x \log L_{\text{IR}} - C_x & \text{for } \text{SFR} < 8 M_{\odot} \text{ yr}^{-1} \\ \log L_{\text{IR}} - C_x & \text{for } \text{SFR} > 8 M_{\odot} \text{ yr}^{-1} \end{cases} \quad (8)$$

In Table 2, we include the best-fit parameters for SFRs based on L_{IR} scaled from the F1800W or F2100W photometry for reference. As before, we suggest that the break at $8 M_{\odot} \text{ yr}^{-1}$ can be substituted with $\log M_{\star}/M_{\odot} = 10.1$. This is discussed further in Section 6.1.

5.3.2. Composite SFR Indicators

Composite SFR indicators combine a direct UV or optical tracer of unobscured emission from young stars with an infrared tracer to capture the missing component absorbed and re-radiated by dust. This method is more robust against the systematic uncertainties introduced by using e.g. the UV or IR alone and so has a long history in the literature (e.g., Kennicutt et al. 2009; Hao et al. 2011; Kennicutt & Evans 2012). It is particularly important in our sample, which spans the range in stellar mass where the obscured SFR component varies from $\sim 20 - 90\%$ (Whitaker et al. 2017). We adopt the common prescription of the form

$$\log \text{SFR} = \log(L_{\text{UV}} + b_x L_{\text{IR}}^x) - \log C_x \quad (9)$$

which is valid under assumptions of energy balance for direct tracers where the attenuation for the continuum or line emission in the UV/optical is similar to the mean dust opacity of the starlight heating the dust (see discussion in Kennicutt et al. 2009). As this is not the case for Pa α (Kennicutt et al. 2009) and the UV can be measured from e.g. HST photometry, we focus on UV+IR composite relations. We measure the rest-frame near-UV at 2300 Å from our SED-fitting (Section 3.2), which is bracketed across our redshift range by the F435W and F606W/F775W HST bands. For easy reference to the literature, we will also look at the far-UV at 1600 Å, though this requires extrapolation.

In Figure 7 (bottom panels), we show the best-fit SFRs as a function of our fiducial SFR_{Pa α} and in Table 2 we list our best-fit parameters. Somewhat surprisingly, we find that Eqn 9 provides an excellent description of our data over its full range, with significantly less scatter (~ 0.15) dex compare to the IR-only calibrations. This indicates that the IR continues to be a robust tracer of the obscured star formation component down to $\log M_*/M_\odot \sim 9$ and total SFRs of $\sim 1 M_\odot \text{ yr}^{-1}$. We further discuss the implications of this in Section 6.1.

The scale factor, b_x , describes the relation between the direct and indirect SFR tracers and in this case is dependent on both the fraction of the dust that is heated specifically by UV photons and the fraction of L_{IR} that is heated by emission related to young stars. Using F1800W – covering the rest-frame $8\mu\text{m}$ – and NUV we find $b_{\text{F1800W}} = 0.08 \pm 0.01$, somewhat lower than calibrations based on local galaxies (Hao et al. 2011; Kennicutt & Evans 2012). Our best fit parameters for Eqn 9 for all four MIRI filters and the NUV at 2300 Å and FUV at 1600 Å are found in Table 3.

5.3.3. The obscured fraction and further verification of our template assumption

Building on our composite SFR calibration presented in the previous section, in Figure 8 (left) we show the obscured SFR fraction, defined as $f_{\text{obs}} \equiv b_x L_{\text{IR}}/L_{\text{NUV}} + b_x L_{\text{IR}}$, as a function of stellar mass. As in previous studies, we find

high f_{obs} at high mass, followed by a steep decline with decreasing mass. However, our fall off is sharper than the main relation presented in Whitaker et al. (2017) based on MIPS stacking. As shown in that work, this is related to the dust emission template used. Whitaker et al. (2017) compared their assumed template, a log-averaged IR template from Dale & Helou (2002, see also Wuyts et al. (2008); Wuyts et al. (2011)), to alternative templates from Kirkpatrick et al. (2015) and Magdis et al. (2012), finding the latter produced a steeper drop off (shown as the black dash-dot line in Figure 8 [left]). In this work, we have assumed the $\log L_{\text{IR}} = 11.25$ template from Rieke et al. (2009), which is similar to the Kirkpatrick et al. (2015) template and produces a similar best-fit relation.

Which assumption is correct? In Figure 8 (right), we test these templates by deriving the f_{obs} independently from our UV and Pa α information, where $f_{\text{obs}} \equiv 1 - \text{SFR}_{\text{NUV}}^{\text{uncorr}}/\text{SFR}_{\text{Pa}\alpha}$. $\text{SFR}_{\text{NUV}}^{\text{uncorr}}$ is derived using the NUV calibration from Kennicutt & Evans (2012) and is *not* corrected for dust attenuation⁹. The result is that this independent measure, to first order, supports both template choices with significant scatter.

However, it is important to remember here (and throughout this study) that the UV (and IR) and Pa α can trace very different star formation timescales (Calzetti et al. 2007). Recent simulations have found that the UV in galaxies with constant SFHs will tend to trace similar timescales as the hydrogen recombination lines (~ 10 Myr; Flores Velázquez et al. 2021) due to the continued renewal of O-type stars that can outshine older populations. Stochastic SFHs, on the other hand, can produce UV that traces longer timescales (~ 100 Myr), averaging over the rise and fall of bursty star formation. To test this, in Figure 8 (right), we color code our sources by the Pa α equivalent width (EW, approximated as Pa α divided by the F444W flux), where larger EWs may indicate more bursty SF (e.g., Tran et al. 2020). At $M_*/M_\odot \lesssim 9.5$, the sources that favor the original Whitaker et al. (2017) fit are those with the highest EWs. We propose that these sources are the most likely to overestimate f_{obs} when comparing UV and Pa α due to the timescale mismatch and tentatively conclude that this test supports the steeper decline and our template choice. f_{obs} and the global dust properties of our sample are discussed further in Section 6.1. The UV properties of these high EW Pa α emitters are discussed further in Section 6.2.2.

5.3.4. Comparison to UV- and SED fitting-based SFRs

In Figure 9, we again show the residuals for MS galaxies between our fiducial Pa α SFRs for our L_{IR} and UV+IR composite SFR calibrations (Table 2–3) and compare them to residuals for dust-corrected UV-based SFRs and the SFRs reported our SED fitting (Section 3.2). For the UV, we correct for dust by determining A_{UV} from the best-fit attenua-

⁹ We note that we find qualitatively the same result using FUV with the Reddy et al. (2023a) calibration. We show the NUV here as it is better constrained by our dataset.

Table 3. UV+IR SFR Calibration

Parameter	NUV+ L_{IR} SFR Calibration			FUV+ L_{IR} SFR Calibration		
	b_x	C_x	σ_{NMAD}	b_x	C_x	σ_{NMAD}
$L_{\text{IR}}^{\text{F1280W}}$	0.11 ± 0.02	9.5 ± 0.04	0.16	0.14 ± 0.02	9.6 ± 0.05	0.15
$L_{\text{IR}}^{\text{F1500W}}$	0.10 ± 0.01	9.5 ± 0.04	0.15	0.13 ± 0.02	9.6 ± 0.04	0.17
$L_{\text{IR}}^{\text{F1800W}}$	0.08 ± 0.01	9.5 ± 0.03	0.16	0.11 ± 0.01	9.6 ± 0.04	0.15
$L_{\text{IR}}^{\text{F2100W}}$	0.12 ± 0.02	9.6 ± 0.05	0.17	0.17 ± 0.03	9.7 ± 0.05	0.17

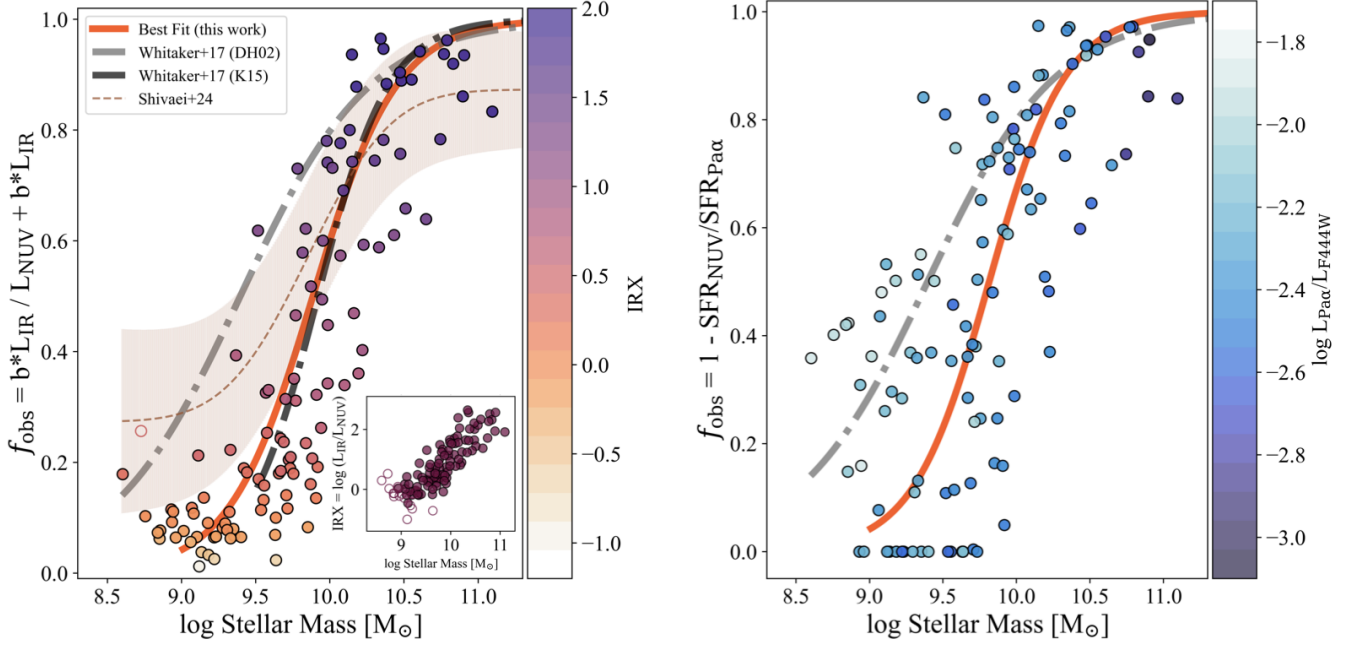


Figure 8. (left) The obscured fraction, f_{obs} , as a function of stellar mass derived from the (uncorrected) NUV and $L_{\text{IR}}^{\text{F1800W}}$ via our derived composite SFR calibration (Eqn 9) for MS galaxies. The dash dot gray and black lines show the fitted relation from Whitaker et al. (2017) based on MIPS stacking plus the Dale & Helou (2002) and Kirkpatrick et al. (2015) IR templates to derive L_{IR} , respectively. The dashed line and shaded region show the fitted relation from Shivaei et al. (2024), based on SED fitting including MIRI broadband photometry. Our best fit is shown as the orange solid line and is in good agreement with Whitaker et al. (2017) when using the Kirkpatrick et al. (2015) templates. The points are color-coded by IRX, which is also shown as a function of stellar mass in the inset. (right) Same as the left panel, only with f_{obs} derived using the SFR_{UV} and $\text{SFR}_{\text{Pa}\alpha}$. Sources with $\text{SFR}_{\text{UV}} > \text{SFR}_{\text{Pa}\alpha}$ have had their f_{obs} set to zero (see Section 6.2.2). The points are color-coded by the ratio of the Pa α to F444W luminosities, as a proxy for the Pa α EWs.

tion curves from SED fitting. We verify that this correction is in good agreement with applying the average SMC attenuation curve from Gordon et al. (2024), which has been found to well describe the UV attenuation in Pa α emitters (Reddy et al. 2023a). We show two UV-based SFR calibrations: 1) for rest 1600 Å, we apply the metallicity-dependent FUV-SFR conversion from Reddy et al. (2023b) and 2) at rest 2300 Å the NUV-SFR conversion from Kennicutt & Evans (2012). We find that the UV-based SFRs have similar scatter to the L_{IR} -based SFRs ($\sim 0.2 - 0.3$ dex). The FUV shows signs of being slightly systematically underestimated by ~ 0.05 dex, potentially related to the assumed attenuation corrections. In

the rightmost panel, we additionally show the SFRs derived from SED fitting (e.g., Leja et al. 2019b) over timescales of 10 and 100 Myr. The former is comparable to the timescales traced by Pa α and the latter with the UV and IR, modulo variations in SFH (e.g., Flores Velázquez et al. 2021). Both appear overestimated (by ~ 0.1 dex) with the $\text{SFR}_{10\text{Myr}}$ estimates being more overestimated at higher masses and having an overall scatter of 0.3 dex. The scatter for $\text{SFR}_{100\text{Myr}}$ is comparable to the UV and IR-based measurements, all of which exceed the scatter for the composite UV+IR SFRs (~ 0.15 dex).

6. DISCUSSION

In this work, we have combined the unprecedented sensitivity of JWST/MIRI imaging with NIRCam’s access to the near-infrared Pa α emission line, the gold standard in SFR indicators, to assess the use of the mid-IR as a SFR tracer in typical, main sequence galaxies at cosmic noon. We find that the rest-frame $8\mu\text{m}$ luminosity – as probed by the MIRI F1800W and F2100W bands over $1 \lesssim z \lesssim 1.7$ – declines steeply at $\text{SFR}_{\text{Pa}\alpha} \lesssim 8 M_{\odot} \text{ yr}^{-1}$, such that $L_{8\mu\text{m},\text{rest}} \propto \text{SFR}_{\text{Pa}\alpha}^{2.2 \pm 0.3}$ (Section 5.1). This is in sharp contrast to the unity-slope relation between the mid-IR and SFR in high mass, high metallicity galaxies at $1 \lesssim z \lesssim 3$ (e.g., Rujopakarn et al. 2013; Shipley et al. 2016).

Fitting our full calibration sample of MS galaxies with a broken power-law with a unity-slope above $8 M_{\odot} \text{ yr}^{-1}$ results in a well behaved $L_{8\mu\text{m},\text{rest}}$ -SFR two-component function with a scatter of 0.33 dex (Figure 6). Likely contributing to this scatter are differences in the transmission curves of the MIRI filters and potential contributions from the rapidly changing spectral features over our redshift range (Figure 2), which we have not controlled for in this first analysis. An additional source of scatter may be the combination of multiple sources of emission (i.e. PAH, hot dust continuum, stellar continuum, and/or AGN) contributing to the MIRI photometry, which we will not attempt to disentangle in this study. Inverting this relation, we provided purely empirical SFR calibrations based on the observed F1800W and F2100W photometry (Eqn 7, Table 1).

In Section 5.3, we expand our calibration to use MIRI single-band photometry to predict the total infrared luminosity, L_{IR} , based on dust emission templates. We find that a single representative template can produce an L_{IR} -SFR relation with slightly lower scatter than the $L_{8\mu\text{m},\text{rest}}$ -SFR relation that makes no assumptions about the SED shape; the implications of this are discussed further below. We presented the SFR calibrations using L_{IR} derived from single-band MIRI photometry in F1280W, F1500W, F1800W, and F2100W in Table 2. These calibrations are two-component and assume a breakpoint in SFR or, equivalently, stellar mass. The latter assumption we review as part of a broader discussion on the L_{IR} -SFR relation in MS galaxies in the next section. From the single-band L_{IR} predictions, we further construct a composite SFR indicator (e.g., Kennicutt & Evans 2012) combining the UV based on SED fitting constrained by HST photometry with the L_{IR} , calibrated against the Pa α SFRs (Eqn 9, Figure 7). Like previous composite SFR indicators, we find our data is well fit by a linear combination of UV+IR, with a tight scatter of < 0.2 dex.

These results demonstrate that, although the mid-IR does display different behavior in less massive and less metal-rich MS galaxies at cosmic noon, single-band imaging of the rest frame $8\mu\text{m}$ or $6\mu\text{m}$ (Section 5.2) spectral regions with JWST/MIRI can be used as a robust SFR indicator down to $\log M_{*}/M_{\odot} \sim 9$. Our parameterization of the composite UV + IR SFR follows the well-established literature and indicates

that the energy balance arguments underlying that functional form still hold.

In the following section, we examine the behavior we’re observing in the mid-IR in terms of the PAH-specific and global dust properties of our galaxies. Then in Section 6.2, we take a closer look at how our calibrations perform in terms of non-MS populations and outliers.

6.1. Photometric SFR Calibration at Rest $8\mu\text{m}$ from Local to Cosmic Noon Galaxies

Given the relative sensitivity and spatial resolution compared to the far-IR, mid-IR SFR tracers have been well-studied in both local and high mass, high SFR galaxy populations up to cosmic noon. The rest-frame $8\mu\text{m}$ spectral region has been particularly targeted due to the convenient coverage by Spitzer IRAC Ch4 locally and MIPS24 at $z \sim 2$ (Díaz-Santos et al. 2008). Broadband measurements, as used in this work, combine PAH emission with continuum emission from hot dust, older stellar populations, and AGN, if present. PAHs scale with the total dust emission, though with a scatter that depends on metallicity, ionization state, the SFR surface density, and age distribution of the stellar population (e.g., Helou et al. 2001; Alonso-Herrero et al. 2004; Engelbracht et al. 2005, 2008; Madden et al. 2006; Draine & Li 2007; Smith et al. 2007; Galliano et al. 2008; Elbaz et al. 2011; Magdis et al. 2013; Egorov et al. 2023; Pedrini et al. 2024) For integrated studies of massive, luminous galaxies without AGN, this variation is minimal (up to ULIRGs; Pope et al. 2008; Wu et al. 2010; Fiolet et al. 2010; Pope et al. 2013; Shipley et al. 2016, see Section 7) and thus the rest $8\mu\text{m}$ can be used as an (obscured) SFR tracer (Alonso-Herrero et al. 2006; Farrah et al. 2007; Pope et al. 2008; Treyer et al. 2010; Pope et al. 2013; Rujopakarn et al. 2013; Kennicutt et al. 2009; Shipley et al. 2016), with the obscured SFR component found to provide a large portion ($\gtrsim 80\%$ at $\log M_{*}/M_{\odot} \gtrsim 10$) of the total SFR, roughly independent of redshift up to $z \sim 2.5$ (Whitaker et al. 2017; Zimmerman et al. 2024).

In this work, we have shown a steep decrease in the $8\mu\text{m}$ emission of MS galaxies at $z \sim 1.3$ below $\text{SFR} \sim 8 M_{\odot} \text{ yr}^{-1}$, a departure from the behavior of previous IR-based SFR indicators. For our SFR calibrations to be applicable over a wide redshift range, we need to now understand what drives this break and decline and whether our calibration needs to evolve with redshift. We can easily rule out that SFR is the fundamental property setting the break; unity-slope relations between $L_{7.7\text{PAH}}$ and SFR have been shown over the range $\sim 0.3 - 30 M_{\odot} \text{ yr}^{-1}$ in more massive galaxies at $z \sim 0.4$ (Shipley et al. 2016). The next logical option is stellar mass and, specifically, its correlation with metallicity. Studies of metal-poor HII regions and low- Z local galaxies (Calzetti et al. 2007; Engelbracht et al. 2005, 2008; Smith et al. 2007; Hunt et al. 2010; Rémy-Ruyer et al. 2015; Chasnet et al. 2019; Aniano et al. 2020) and $z \sim 2$ (Shivaei et al. 2024) galaxies have found deficits in the rest-frame $8\mu\text{m}$, often attributed to a decrease in PAH abundance relative to L_{IR} at sub-solar metallicities.

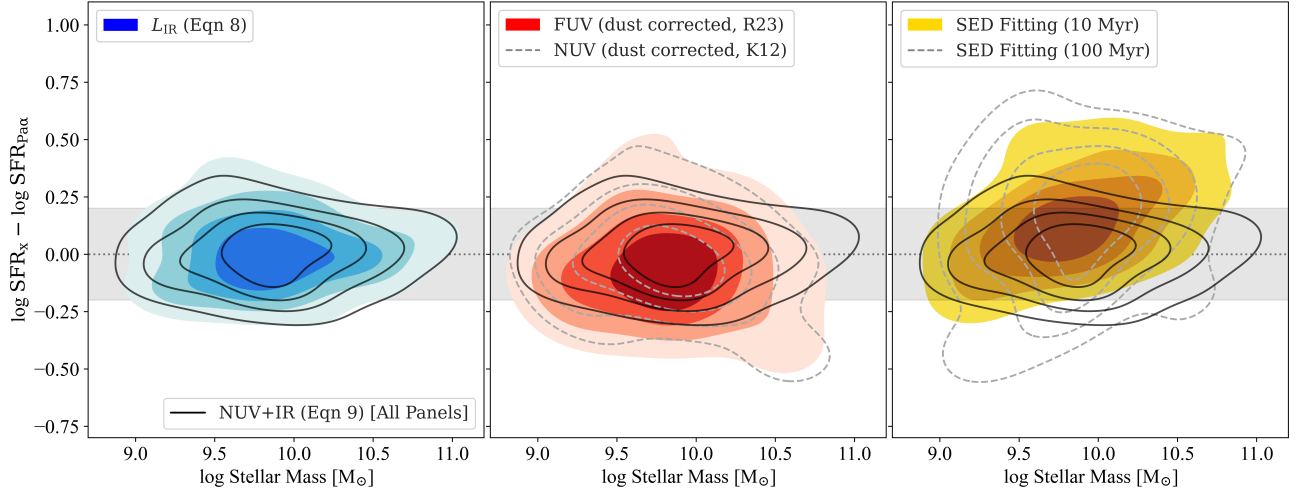


Figure 9. The residuals between SFRs calculated through different methods and the fiducial $\text{Pa}\alpha$ SFRs. In all panels the residuals for the UV+IR composite SFR calibration (Eqn 9, Table 3) are shown as solid black contours. (left) The blue color contours show the L_{IR} -based SFR (Eqn 8, Table 2). (middle) The red color and dashed line contours show dust corrected UV-based SFRs from the FUV (Reddy et al. 2023b) and NUV (Kennicutt & Evans 2012). (right) The yellow color and dashed line contours show the best-fit SFRs from `Prospector` over timescales of 10 and 100 Myr.

However, stellar mass is also positively correlated with global dust properties, such as dust obscuration. In the next two sections, we consider whether the behavior we see in the $L_{8\mu\text{m}}$ -SFR relation is better described by a decrease in PAH abundance specifically, or a lower (global) dust obscuration, and discuss the implications for our calibration.

6.1.1. MIR dust emission at low stellar mass ($\log M_*/M_\odot < 10$) and metallicity

The deficit of PAHs at low metallicity is well established in the literature, though the details remain unclear. Some studies find that the PAH abundance drops sharply at $\sim 0.2 - 0.3 Z_\odot$ (Engelbracht et al. 2005, 2008; Smith et al. 2007; Draine & Li 2007; Chastenet et al. 2019; Shim et al. 2023) while others find a more continuous decline at $\sim 0.5 - 0.7 Z_\odot$ (Galliano et al. 2008; Rémy-Ruyer et al. 2015; Aniano et al. 2020; Whitcomb et al. 2024; Shivaei et al. 2024). In this work, we see a decline in $L_{8\mu\text{m},\text{rest}}$ beginning at $\text{SFR} = 8 M_\odot \text{ yr}^{-1}$, which for a MS galaxy at $z \sim 1.3$ corresponds to $\log M/M_\odot \sim 10.1$. Adopting the mass-metallicity relation at this redshift from Topping et al. (2021) and the O3N2-metallicity calibration from (Bian et al. 2018), this corresponds to a metallicity of $\sim 0.7 Z_\odot$. This appears consistent with studies that find a continuous decline.

However, it's important to remember that this decline may not affect all of the PAH features equally and we are particularly interested in the 6.2 and 7.7 μm PAHs. A lower PAH abundance is often attributed to either photodestruction of small grains in e.g. hard radiation fields or inhibited large grain growth due to lack of metals. Using Spitzer IRS spectroscopy, Smith et al. (2007) observed PAH feature ratios consistent with power shifting from long to short wavelength PAH bands with decreasing metallicity, indicating that large grain growth is inhibited at low Z . The 6.2 and 7.7 μm fea-

tures, comprised of relatively smaller grains, were less affected (see also Hunt et al. 2010; Sandstrom et al. 2012). In three nearby spirals, Whitcomb et al. (2024) confirmed that while the general trend is of decreasing total PAH luminosity with decreasing metallicity, the most rapid decrease is in the large grain 17 μm PAH feature, with the 7.7 μm PAH showing a more gradual decrease and the 6.2 μm PAH actually showing a modest increase.

A decrease in the abundance of the grains that create the 7.7 μm emission complex would imply that our breakpoint and decline is tied directly to metallicity. As a result, it would evolve with redshift following the mass-metallicity relation. Our analysis, however, suggests this is not the case. In Section 5.3, we derived a UV+ L_{IR} SFR calibration using the common functional form (Eqn 9), which is built on the assumption of energy balance between UV photons associated with star formation and dust attenuation. Crucially, we derived the L_{IR} using a single IR template with a fixed $L_{8\mu\text{m},\text{rest}}$ to L_{IR} ratio (Section 5). If the 7.7PAH to L_{IR} ratio was decreasing smoothly, we would expect to systematically underestimate the L_{IR} by factors of $\gtrsim 2$ at the low mass end of our calibration sample. This would violate energy balance and not result in the linear UV+IR relation we derive.

6.1.2. Global dust emission at low mass: the obscuration fraction sets the breakpoint

Given the discussion above, we next consider the global dust properties — dominated by large grains in thermal equilibrium — at low metallicity. Global dust properties are, of course, also sensitive to metallicity, which will lower the dust-to-gas ratio and cause changes of the radiation field, which affects the dust equilibrium temperature. A curious thing, then, is that it has been established that the obscuration fraction, f_{obs} , at fixed stellar mass has weak or no evolution

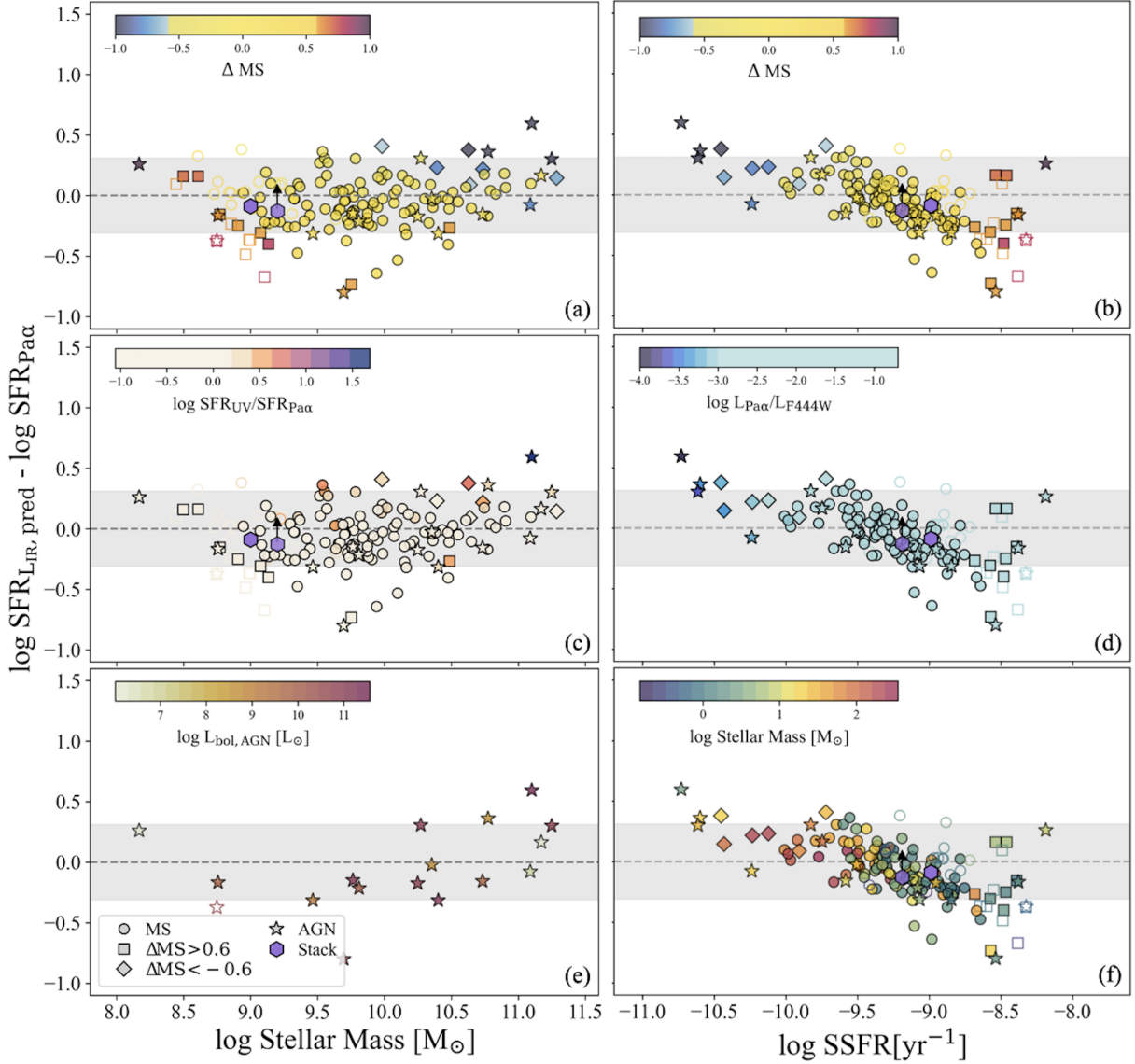


Figure 10. The residuals in dex between the predicted SFR from our L_{IR} -based SFR calibration (Eqn 8, Table 2) as a function of stellar mass (left panels) and SSFR (right panels). Solid (open) symbols are detections ($\text{SNR} < 3$) in F1800W. Circles, squares, diamonds, and stars show MS, above MS ($\Delta\text{MS} > 0.6$), below MS ($\Delta\text{MS} < -0.6$), and AGN, respectively. The shaded regions show a scatter of 0.3 dex, determined using the MS galaxy sample. Different galaxy properties and potential sources of scatter are highlighted in different panels: (a-b) galaxies are colored accounting to whether they are on, above, or below the MS; (c) highlights sources with excess UV defined as $\text{SFR}_{2300\text{\AA}}^{\circ}/\text{SFR}_{\text{Pa}\alpha} > 2$ (Section 6.2.2); (d) highlights sources with low Pa α to continuum luminosities, measured in the F277W filter (Section 6.2.3); (e) shows AGN and their bolometric luminosities (Section 6.2.4); and (f) shows the trend with SSFR while highlighting the stellar mass.

with redshift up to $z \sim 3$ (Bouwens et al. 2016; Whitaker et al. 2017; McLure et al. 2018; Shapley et al. 2022). Recent cosmological simulations (Zimmerman et al. 2024) suggest that f_{obs} actually does increase with redshift (at fixed mass), which could potentially counter the effects of decreasing metallicity and create the illusion of weak or no evolution. This increase is attributed to changing star-dust geometry (Zimmerman et al. 2024), as the well characterized $M_{\text{dust}} - M_{\star}$ relation and gas-to-dust ratio-metallicity relation doesn't seem to evolve with redshift (Popping & Péroux 2022; Zhang et al. 2023).

In Figure 8 (left), we show the f_{obs} derived from our UV+IR calibration as a function of stellar mass. As established in previous works (e.g., Whitaker et al. 2017), we see an asymptote toward $f_{\text{obs}} \sim 0.8 - 1$ at high masses, followed by a steep decline with large scatter at fixed stellar mass. Via the colorbar and inset, we show the infrared excess, $\text{IRX} \equiv L_{\text{IR}}/L_{\text{UV}}$, for our sample. IRX is known to be tightly correlated with stellar mass (e.g., Bouwens et al. 2016) and simulations confirm that IRX is a strong proxy for the effective UV opacity, which is set by the column density of dust relative to young stars (Popping et al. 2017;

Narayanan et al. 2018; Liang et al. 2021). Together IRX and dust mass, also tightly correlated with stellar mass, set f_{obs} .

The drop in $L_{8\mu\text{m,rest}}$ following the drop in the global f_{obs} naturally sets a non-evolving breakpoint in stellar mass through the $f_{\text{obs}}-M_*$ relation up to $z \sim 3$. Global dust properties driving this trend as opposed to a drop in the $7.7 \mu\text{m}$ (or $6.2 \mu\text{m}$) PAH abundance is consistent with our assumption of a single dust template and our UV+IR composite SFR, which obeys energy balance. It further supports our use of the $6.2 \mu\text{m}$ PAH to extend the redshift range for MIRI-based SFRs to ~ 3 and suggests that our calibration is not overly sensitive the fraction of the 6.2 or $7.7 \mu\text{m}$ captured within a given MIRI filter. As such, we conclude that our MIRI-based SFR calibration (Eqn 8, Table 2) can be applied to MS galaxies over a wide redshift range.

6.2. Understanding the Outliers and Broader Applicability of MIRI-based SFRs

In Figures 10 and 11, we show the residuals of our predicted SFRs relative to $\text{SFR}_{\text{Pa}\alpha}$ from our L_{IR} (Eqn 8) and UV+IR (Eqn 9) calibrations, respectively. Predicted SFRs are calculated using the F1800W photometry and the FUV from our SED fitting. These residuals are shown as a function of stellar mass (left) and the instantaneous SSFR (right), calculated using $\text{SFR}_{\text{Pa}\alpha}$. The top two panels (a-b) display the full population – MS, above/below MS, and AGN – while the remaining panels (c-f) highlight different populations and potential sources of scatter.

6.2.1. (UV+)MIRI-based SFRs in high SSFR and Starburst galaxies

In Figure 10, the residuals between our L_{IR} -based SFRs and the fiducial $\text{Pa}\alpha$ SFRs overall show weak to no trend with stellar mass (panel a) but some dependence on SSFR (panel b), with our SFR calibrations tending to over-predict at low SSFR and under-predict at high SSFR. Starburst galaxies, defined as $\delta\text{MS} > 0.6$, mostly fall below the scatter we have measured for our MS population. In Figure 11 (panel b), we see that this trend in the residuals with SSFR is much less obvious among MS galaxies; however, starbursts mostly remain outliers.

SSFR has been found to track the average radiation field, even on galaxy-integrated scales, and is anti-correlated with both q_{PAH} (Chasteney et al. 2025) and IRX (Figure 8). Interestingly, the colorbar in Figure 10 (panel f) shows that the high SSFR and starburst outliers range in mass, and thus metallicity, which is consistent with the lack of strong trend in the residual outliers with mass and emphasizes the role of the SSFR and by proxy the radiation field in setting the $L_{8\mu\text{m,rest}}/L_{\text{IR}}$ (e.g., Elbaz et al. 2011; McNulty et al. 2026). As some of this trend with SSFR weakens and some (namely in the starburst population) remains when the UV is added into the predicted SFR, we posit that both a decrease in PAH abundance due to high radiation fields (e.g., Baron et al. 2025) and a change in global dust properties via star-dust geometry could be contributing to the intrinsic MS scatter and this outlier population.

6.2.2. High predicted (UV+)MIRI-based SFRs in galaxies: UV excess?

A comparison of Figures 10 and 11 highlights a particular set of outliers in our MS calibration sample at $\log M_*/M_\odot \sim 9-9.5$ that have elevated UV+IR SFRs. In panel c in these two figures, we explore this by looking at the ratio of the SFR derived solely from the *uncorrected* UV, e.g. presumably tracing the unobscured star formation component, versus the $\text{Pa}\alpha$ SFR. To derive the UV SFR, we adopt the metallicity-dependent calibration presented in Reddy et al. (2023b), which is based on the same models as the their $\text{Pa}\alpha$ SFR calibration. We find that these outliers have high UV-based SFRs, $\sim 2-5\times$ the $\text{Pa}\alpha$ SFR¹⁰.

A possible explanation is provided by recent simulations with FIRE-2 (Flores Velázquez et al. 2021), which found that the FUV in galaxies with constant SFHs can trace short timescales (~ 10 Myr) similar to hydrogen recombination lines ($\sim 5-10$ Myr; Hao et al. 2011; Flores Velázquez et al. 2021) due to the continued renewal of O-type stars that can outshine older populations. In galaxies with stochastic SFHs, however, the UV can stay elevated for longer timescales ($\gtrsim 100$ Myr; see also Murphy et al. 2011; Kennicutt & Evans 2012; Calzetti 2013) following the lull after a burst. This is consistent with studies finding increased scatter between UV- and Balmer line-based SFRs in low mass galaxies (Domínguez et al. 2015; Guo et al. 2016; Emami et al. 2019; Atek et al. 2022; Cleri et al. 2022; Reddy et al. 2023a, 2025), which are increasingly thought to have stochastic SFHs (Navarro-Carrera et al. 2026). This highlights that the timescales and other factors that may influence UV-based SFR calibrations need to be considered, particular as JWST has opened up access to the UV in high- z , low mass populations.

6.2.3. High predicted (UV+)MIRI-based SFRs in galaxies below the MS: contributions from evolved stellar populations?

In the previous section, we discussed galaxies where the predicted UV SFR is higher than the $\text{Pa}\alpha$ SFR, potentially owing to the different timescales being traced and stochastic SFHs. Similarly, the timescale over which the IR traces SFR can have a complex relationship with SFH (Calzetti et al. 2025, and references therein) and, importantly, the IR can additionally include contributions from evolved stellar populations largely unrelated to recent star formation (e.g., Crocker et al. 2013; Calapa et al. 2014; Fumagalli et al. 2014; Hao et al. 2011). Low $L_{8\mu\text{m}}$ to $L_{\text{Pa}\alpha}$ ratios have been found to be associated with smaller $\text{Pa}\alpha$ EWs in local, resolved studies, signaling older stellar ages (Díaz-Santos et al. 2008). In Figures 10 and 11 [panels a, b], we see that galaxies below the MS ($\Delta\text{MS} < -0.6$) — which we note do not satisfy UVJ quiescent galaxy selection and so are not classified as quenched — tend to inhabit the upper end of our scat-

¹⁰ We only consider UV SFR excesses above $\text{Pa}\alpha$ SFRs of $> 2\times$ to be conservative against calibration uncertainties.

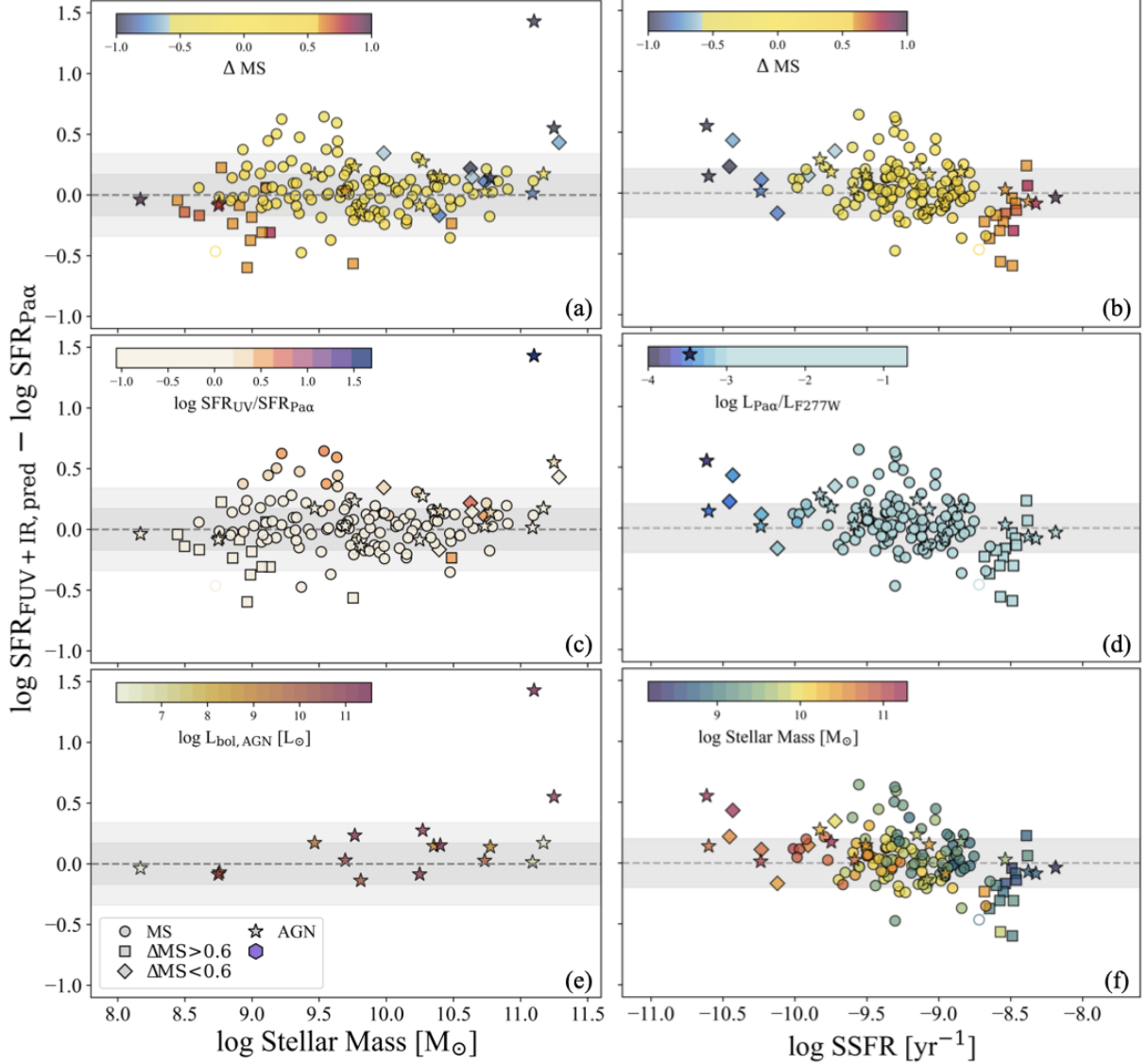


Figure 11. As in Figure 10, except showing the residuals for the UV+IR based SFRs (Eqn 8, Table 3).

ter, though only one is a $> 2\sigma$ outlier in the UV+IR SFRs. In panel d, we show that low SSFR sources in our sample have low Pa α equivalent widths, $3 - 10\times$ lower than the median ratio. This suggests our overestimated predicted SFRs in low SSFR sources are boosted by contributions from evolved stars in the IR (or AGN, see Section 6.2.4). However, our subsample of sub-MS galaxies is generally within our scatter and small, including only 6 galaxies. Among MS galaxies, we cannot rule out excess IR emission from evolved populations contributing to our overall scatter and indeed this could contribute to the correlation we see between L_{IR} -based SFRs and SSFR in Figure 10.

6.2.4. (UV+)MIRI-based SFRs in AGN

In Section 5, we removed AGN from our calibration sample as AGN emission can contaminate the Pa α emission line (e.g., Sun et al. 2025) as well as the UV and mid-IR contin-

uum. For moderately luminous AGN, however, the host contribution may still dominate and in highly obscured AGN, the contributions to the UV, optical, and mid-IR can be minimal (Kirkpatrick et al. 2015; Lyu et al. 2024; Kirkpatrick et al. 2023). In these cases, our calibration may still provide a first order estimate of the star formation rate.

In Figures 10 and 11 (panel e), we examine the residuals between our L_{IR} - and UV+IR-based SFR calibrations and the Pa α SFRs for previously identified AGN (Section 3). We find that most of our AGN fall in the expected scatter for non-AGN MS calibration sample. We have two significant ($> 2\sigma$) outliers with high predicted UV+IR SFRs (Figure 11). Both are luminous X-ray AGN (Lyu et al. 2022) in massive hosts. The most extreme outlier was additionally identified in Sun et al. (2025) as having a broad component to its Pa α line. Their selection in the X-ray and optical indicates they are unobscured AGN, which is consistent with their UV+IR SFRs

being significantly more overestimated than their L_{IR} -based SFRs. In our sample, five additional X-ray-selected AGN in more intermediate mass hosts fall within our calibration’s scatter.

We additionally have one outlier with a low L_{IR} -based SFR. This AGN was identified in the mid-IR (Lyu et al. 2024) and via its X-ray to radio ratio (Alberts et al. 2020; Lyu et al. 2022) and has an AGN bolometric luminosity of $\log L_{\text{AGN}}/L_{\odot} = 10.8$. Its UV+IR SFR, however, is again within our scatter. At a more intermediate mass ($\log M_{\star}/M_{\odot} = 9.8$), this AGN may have a host weak in the IR and/or the AGN could be contributing to the Pa α and UV. Disentangling these is beyond the scope of this work.

In general, our SFR calibration provides SFR estimates in AGN candidates that are still within the scatter derived from the non-AGN calibration sample for the bulk of these AGN (14 out of 17). Given this, we suggest that our calibration can be applied to AGN-hosting galaxies and that comparing L_{IR} -based and UV+IR SFRs can help identify outliers.

7. Pa α AND IR-BASED SFRS IN LUMINOUS INFRARED GALAXIES

MIRI’s capabilities now give us unprecedented coverage of the mid-IR beyond the local Universe, allowing us to individually detect galaxies where previously we had to rely on stacking. In the previous sections, we calibrated MIRI- and UV+IR-based SFR indicators against the Pa α emission line in MS galaxies at cosmic noon. Our sample was comprised of galaxies with low- to moderate-infrared luminosities ($\log L_{\text{IR}}/L_{\odot} \sim 9 - 11.5$), a result of the relatively small MIRI FOV compared to the surveying power of e.g. Spitzer. As such, we relied on previous studies to parameterize our calibration at higher luminosities and SFRs. However, as MIRI (and grism) surveys accumulate more area (for example, the PRIMER and MINERVA MIRI surveys will cover over 250 arcmin², see Muzzin et al. 2025), we will be able to examine the bright populations previously probed during the Spitzer era with the finer detail provided by MIRI’s sensitivity and resolution. Here we combine data from previous missions like Spitzer and Herschel with new JWST observations to discuss Pa α and IR-based SFRs in galaxies with $\log L_{\text{IR}}/L_{\odot} \gtrsim 11 - 13$.

7.1. PAH behavior at high luminosities

The ratio of PAHs to the total infrared luminosity is known to drop sharply at high L_{IR} , starting at a threshold of $\log L_{\text{IR}}/L_{\odot} \sim 12$ locally (Shipley et al. 2016). This implies that PAHs may no longer track the obscured SFR at these luminosities. However, quantifying and explaining this drop has historically been challenging due to potential contamination from heavily obscured AGN. New analyses with JWST now allow us to revisit this issue based on improved tools for quantifying the contribution from AGN to the mid-IR in these extreme galaxies. In Rieke et al. (2025), NIRSpec and MIRI IFU observations of four local ULIRGs put strong upper limits on high excitation AGN lines such as [NeVI], indicating that AGN in local ULIRGs can be so deeply embed-

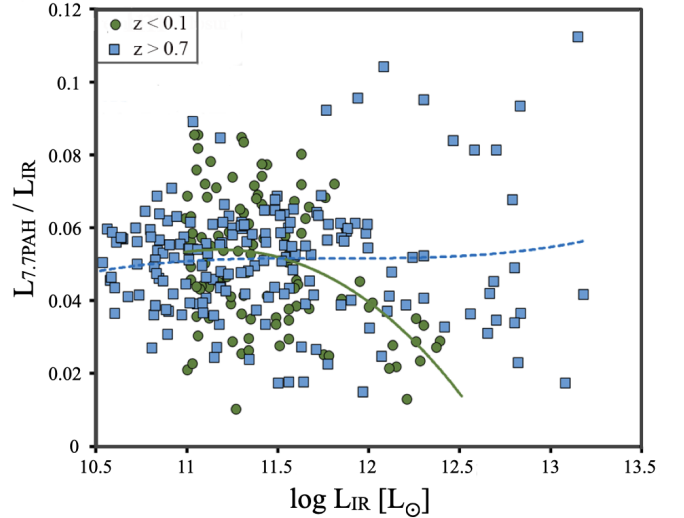


Figure 12. Ratio of the 7.7 μm PAH luminosity to the total infrared luminosity. The green dots are for galaxies at $z < 0.1$, and the green solid line is a 3rd order fit to them. The blue squares are for galaxies at $z > 0.7$ and the blue dashed line is a 3rd order fit.

ded and/or their accretion so intermittent that the AGN is not contributing to the mid-IR spectrum. An examination of the dynamics and black hole masses of a larger ULIRG sample found a large fraction have low Eddington ratios. Taken together, this indicates that, contrary to previous models, the mid-IR in many ULIRGs is powered by star formation, allowing us to examine the PAH deficit in this context.

Based on the analysis in Rieke et al. (2025) outlined above, we re-examine the PAH abundance in local and high- z LIRGs and ULIRGs to assess the mid-IR as a SFR indicator. In Figure 12, we show the $L_{7.7\text{PAH}}/L_{\text{IR}}$ ratio from the GOALS sample (Stierwalt et al. 2014) at $z < 0.1$. The 7.7 μm PAH fluxes were derived from Spitzer IRS spectra and are equivalent to those measured using the standard PAH modeling tool PAHFIT (Smith et al. 2007). We take the total infrared luminosities derived from IRAS photometry from Sanders et al. (2003). We note U et al. (2012) demonstrated that adding longer wavelength data does not significantly modify the L_{IR} estimates. We discard measurements of close pairs, where the Spitzer/IRS spectra and the IRAS photometry may not refer to the same region/galaxy. To be conservative, we also discard cases where an AGN has plausibly affected the PAH features, based on the full SED.

Our compilation of local galaxies agrees with the trends found in previous studies (e.g., Shipley et al. 2016; Lai et al. 2020). Namely, in local ULIRGs, the average $L_{7.7\text{PAH}}/L_{\text{IR}}$ ratio is about half the average value for the $11 < \log L_{\text{IR}}/L_{\odot} < 11.5$ sample. This drop apparently starts at $\log L_{\text{IR}}/L_{\odot} \sim 11.5$ and becomes dramatic for $\log L_{\text{IR}}/L_{\odot} > 12$, albeit with significant scatter. The behavior over the full range of luminosity appears to be relatively well

behaved, making it tempting to fit the trend¹¹ as a correction term for local ULIRG measurements.

This behavior is known to be substantially reduced at even modest redshift (Rujopakarn et al. 2013) with a roughly constant ratio reported up to $\log L_{\text{IR}} \sim 12.5$ at $z \gtrsim 0.7$ (Shipley et al. 2016). To construct an improved high redshift comparison sample, we proceed as follows, with results plotted in Figure 12. For the lower luminosities, $\log L_{\text{IR}}/L_{\odot} \lesssim 11.5$, we again take advantage of SMILES over a larger redshift range, adopting values for $L_{7.7\text{PAH}}$ and L_{IR} from Shivaie et al. (2024). These were estimated through full UV to IR SED fitting, assuming energy balance. We note that the priors used in Shivaie et al. (2024) may be too restrictive to fully model the mid-IR dust (McNulty et al. 2026) and only a small fraction of sources had far-IR constraints on the L_{IR} . As such, we do not attempt to interpret the scatter in the measurement of the ratio, we only assess the qualitative trend in the $L_{7.7\text{PAH}}/L_{\text{IR}}$ ratio with increasing infrared luminosity. To compare this and the local sample with a consistent calibration, we renormalize such that the Shivaie et al. (2024) sample’s average ratio matches the best-fit average for local galaxies from Shipley et al. (2016, their Eqn 21).

For the higher luminosities, we take values from the literature thought to be from star formation-dominated galaxies (Sajina et al. 2007; Rigby et al. 2008; Huang et al. 2009; Pope et al. 2013; Shipley et al. 2016). All PAH measurements were made in a way consistent with the PAHFIT approach. Those reported relative to the local continuum were corrected by a factor of 1.7 as found compared to a spline-based decomposition (e.g., Pope et al. 2013) There are a number of other samples with Spitzer IRS spectra, but they were not included if they used the PAHs as their primary means to identify AGN (e.g., Dasyra et al. 2009; Fiolet et al. 2010). Nonetheless, there are likely some cases in our high luminosity sample with significant AGN power, which would lower their $L_{7.7\text{PAH}}/L_{\text{IR}}$ ratio. Since Figure 12 illustrates that this sample on average has larger values of this ratio than do local high-luminosity galaxies, this contamination would have no effect on our overall conclusion.

As shown in Figure 12, there is no clear drop in the ratio up to $\log L_{\text{IR}}/L_{\odot} \sim 13$. In addition to measurement uncertainties, one caveat is that some of the apparently very high luminosity cases may be lower luminosity galaxies amplified by gravitational lensing (Spilker et al. 2016). This makes straightforward determination of their luminosities and star formation rates problematic, muddling the interpretation at the very highest luminosities. As such, we conclude there is little evidence for PAH suppression in ULIRGs at cosmic noon, but more sources and more robust measurements are still needed.

¹¹ For $z < 0.1$,

$$\frac{L_{7.7\text{PAH}}}{L_{\text{IR}}} = -0.0025 * w^3 + 0.0646 * w^2 - 0.5058 * w + 1.131 \quad (10)$$

where $w = \log L_{\text{IR}}/L_{\odot}$.

7.2. The behavior of Pa α (and $L_{\text{PAH}}/L_{\text{IR}}$) in local ULIRGs with JWST

Throughout this work, we have assumed Pa α is a “gold standard” of SFR indicators, as initially described in detail in Alonso-Herrero et al. (2006) and Calzetti et al. (2007). These works found that at high luminosities, SFRs from IR increased faster than that from Pa α as quantified in Rieke et al. (2009) for $\log L_{\text{IR}} \gtrsim 11$. Two scenarios emerged: Alonso-Herrero et al. (2006) ascribed this behavior to the dust in the most luminous local galaxies (which contain the densest star forming regions) being able to absorb a higher percentage of the ionizing photons from young stars. In this explanation, the IR gives a more reliable measure of the SFR than Pa α . Calzetti et al. (2007) instead suggested that the dust is hotter in bright galaxies, increasing their output at $24 \mu\text{m}$ while Pa α continues to trace the SFR.

With JWST, we can now revisit this issue. In particular, access to multiple hydrogen recombination lines allows us to correct Pa α for extinction, which can become a significant factor in very luminous galaxies. We look again at the four ULIRGs with JWST/NIRSpec IFU from Rieke et al. (2025, see also Perna et al. (2024) and Goldberg et al. (2024) for details on the data acquisition and line measurements for Arp 220). We correct Pa α for extinction using the Br α or Pfund γ lines, assuming intrinsic ratios given by case B recombination (Hummer & Storey 1987)¹² and an extinction law with $R_V = 3.1$ from Gordon et al. (2021).

We test two geometries. The first is the common assumption that the obscured source is behind a foreground screen. Although this model does not even rise to the level of minimal plausibility for ULIRGs, we list the extinction-corrected Pa α in Table 4 for reference. Secondly, we use a more plausible geometry where the emitting source and obscuring material are mixed. In this case

$$F_{\text{obs}} = F_{\text{intrinsic}} \times \frac{1 - e^{-\tau}}{\tau} \quad (11)$$

where we take τ to be proportional to the wavelength-dependent extinction in the law used in the screen geometry. As shown in the table, the difference in this case is minor, which is expected because τ at Pa α is relatively small, $\sim 2 - 6$. We note the full correction for extinction in ULIRGs is substantially more complex than this approximation (Donnan et al. 2024). However, since our approach is equivalent to basing the recombination line flux on Br α (or Pf γ), even less sensitive to extinction with $\tau \lesssim 1 - 1.5$ these complexities are unlikely to increase the estimated fluxes substantially.

In Table 4, we list the SFRs derived from the extinction-corrected Pa α based on mixed geometry and the conversion

¹² We assume $T_e = 10,000 \text{ K}$ and $N_e = 10^4 \text{ cm}^{-3}$, which are roughly appropriate for the dense gas in a ULIRG nucleus. The line ratios are slightly dependent on these parameters (Hummer & Storey 1987) but this dependence is not enough to affect our conclusions.

Table 4. Star formation rates from infrared spectral features

Galaxy	$f_{\text{Pa}\alpha}$	$f_{\text{P}\beta\gamma}$	$f_{\text{Br}\alpha}$	$f_{7.7\text{PAH}}$	$\log L_{\text{Pa}\alpha}$		$\text{SFR}_{\text{Pa}\alpha}$	$\text{SFR}_{7.7\text{PAH}}$	$\text{SFR}_{L_{\text{IR}}}$
					Fgnd. Screen	Mixed			
Arp 220	15.16	9.23	...	3.73×10^5	37.48	43.0	16	72	244
IRAS 14378	2.76	...	1.11	3612	5.77	5.99	41.5	27	212
IRAS 17208	2.38	...	1.67	2.42×10^5	10.59	14.4	39	65	369
IRAS 23365	1.68	...	0.76	4702	4.11	4.38	28	32	203

NOTE—Columns 2 – 5: Flux densities are given in $10^{-17} \text{ W m}^{-2}$. Hydrogen recombination line fluxes are from [Perna et al. \(2024\)](#) for Arp 220 and [Rieke et al. \(2025\)](#) for the IRAS sources. The $7.7 \mu\text{m}$ PAH flux is from [Stierwalt et al. \(2014\)](#). Columns 6 – 7: extinction-corrected $\text{Pa}\alpha$ luminosities given in W for a foreground screen and mixed geometry, respectively. Columns 8 – 10: SFRs are given in $M_{\odot} \text{ yr}^{-1}$ (see Section 7.2 for details).

rate from [Rieke et al. \(2009\)](#). Converting first to $\text{H}\alpha$ as in [Calzetti et al. \(2010\)](#) gives consistent results. We further list the SFRs as derived from the L_{IR} from [Sanders et al. \(2003\)](#); [U et al. \(2012\)](#), using the conversion given in [Kennicutt & Evans \(2012\)](#). In all cases, the L_{IR} -based SFRs are an order of magnitude larger than those derived from $\text{Pa}\alpha$.

We show similar results for the $7.7 \mu\text{m}$ PAH-based SFRs from the results reported by [Stierwalt et al. \(2014\)](#). We have adopted their L_{PAH} and corrected for the relative contribution of the $7.7 \mu\text{m}$ feature alone, $\sim 56\%$. The estimated SFRs are similar to those from $\text{Pa}\alpha$ perhaps trending somewhat higher, but still far below the values from total infrared luminosity, as expected. If we apply this same mixed model using the derived values of τ from $\text{Pa}\alpha$ and $\text{Br}\alpha$ to the $7.7 \mu\text{m}$ PAH feature, we find that the reduction in its intrinsic flux is of order a factor of 1.3 (1.8 for IRAS 17208). That is, extinction may contribute to its reduced flux in these ULIRG but falls short of accounting for the entire effect.

Returning to the two scenarios, we evaluate the possible explanations for the underestimates of the $\text{Pa}\alpha$ SFR in ULIRGs. The critical region to test whether the dust temperature increases with increasing star formation is $\sim 10\text{--}20 \mu\text{m}$. However, the shapes of the star formation-powered IR SEDs have been found to be remarkably independent of luminosity in this range ([Rieke et al. 2009](#); [Magdis et al. 2012](#)), inconsistent with a change in dust temperature. In comparison, the phenomenon of the dust in very dense regions competing for the ionizing photons is well understood (e.g., [Inoue et al. 2001](#); [Dopita et al. 2003](#)). Additional absorption of ionizing photons could also explain the PAH deficits as the small grain PAHs can be destroyed by photodissociation (e.g., [Egorov et al. 2025](#)). Taken together, this suggests that long-wavelength IR measurements are the best proxy for SFR in these very infrared-luminous galaxies.

7.3. Lessons to apply to cosmic noon

In the two previous sections, we have confirmed the suppression of PAHs seen relative to the L_{IR} in local, highly luminous infrared galaxies (Figure 12; e.g., [Shipley et al. 2016](#)). This behavior, however, appears to disappear even at modest redshifts, indicating that MIRI- and generally IR-

based SFRs are robust in the most luminous infrared sources at cosmic noon. We additionally looked at the behavior of $\text{Pa}\alpha$ in four local ULIRGs – taking advantage of JWST’s coverage of multiple hydrogen recombination lines – and found that extinction-corrected $\text{Pa}\alpha$ can underestimate the SFRs by up to an order of magnitude compared to L_{IR} based on long-wavelength IR data. As with the PAHs, however, this behavior may not be common at cosmic noon: in the local ULIRGs, the suppression of both $\text{Pa}\alpha$ and the PAHs is likely related to the star-dust geometry (as discussed in Section 6.1). Locally, (U)LIRGs host very compact, dense starbursts, while star formation is thought to be more extended during cosmic noon (e.g., [Rujopakarn et al. 2011](#)), which has been recently confirmed by a spatially resolved analysis with MIRI ([Florian et al. 2025](#)). As such, the MIRI-based SFRs derived in this paper, as well as $\text{Pa}\alpha$ SFRs, should be accurate and robust over a large range in luminosity and redshift, with the caveat that care must be taken when applying these measures to i.e. compact starbursts or cases with extremely high luminosity densities in their star forming regions. The latter may be an important population at $5 < z < 7$ ([De Rossi et al. 2018](#)), where extremely high densities of UV luminosity may be reached in star forming regions. These conditions are predicted to be uncommon during cosmic noon ([De Rossi et al., 2026, submitted](#)).

8. CONCLUSIONS

In this work, we have examined the behavior of the mid-IR emission in galaxies spanning four orders of magnitude in total infrared luminosity ($9 \lesssim L_{\text{IR}}/L_{\odot} \lesssim 13$). Our main analysis extends mid-IR-based SFR indicators into the regime previously limited to stacking analyses in the IR, namely MS galaxies at cosmic noon, based on MIRI photometry in the F1280W, F1500W, F1800W, and F2100W filters. To calibrate, we use fiducial SFRs from the extinction-corrected $\text{Pa}\alpha$ emission line, a gold standard SFR indicator (e.g. [Alonso-Herrero et al. 2006](#); [Calzetti et al. 2007](#)). Our sample of 169 galaxies at $1 < z < 1.75$, cross-matched between the SMILES and FRESCO surveys, covers $9 \lesssim \log M_{\star}/M_{\odot} \lesssim 11$, reaching a MS SFR of $\text{SFR} \sim 1 M_{\odot} \text{ yr}^{-1}$, over an order of magnitude below the MIPS $24 \mu\text{m}$

confusion limit at $z \sim 1.3$. Our SFR calibration efforts can be summarized as follows:

- Using a clean calibration sample of MS galaxies (Section 3), we examine the behavior of rest-frame $8\ \mu\text{m}$ emission – dominated by PAHs and probed by MIRI’s F1800W and F2100W filters – relative to the $\text{Pa}\alpha$ emission line. We find the mid-IR luminosity steeply declines ($\alpha \sim 2$) when compared to $\text{SFR}_{\text{Pa}\alpha}$ below $\text{SFR} \sim 8 M_{\odot} \text{ yr}^{-1}$. This is in sharp contrast to the unity relation between the (mid-)IR and SFR in massive galaxies at cosmic noon (e.g. Rujopakarn et al. 2013; Shipley et al. 2016). We fit our full sample with a two-component, broken power-law (Eqn 6) with a variable faint end slope and bright end slope fixed to unity. The latter is necessary based on our small sample size at the bright end, driven by the SMILES area. From this fit, we derive a SFR calibration based purely on F1800W and/or F2100W photometry (Eqn 7, Table 1) with a scatter of $\sim 0.3 - 0.4$ dex.
- **Our main MIRI-based SFR calibration** (Eqn 8, Table 2) builds on the previous analysis by introducing local dust emission templates parameterized by total IR luminosity from Rieke et al. (2009) and scaling the single-band MIRI F1800W or F2100W photometry to measure L_{IR} . We find that using a single, representative template reduces the scatter of our SFR calibration to $\sim 0.2 - 0.3$ dex, on par with previous IR-based SFR calibrations. Introducing multiple templates does not improve our calibration, likely due to the shape of the dust SED not being a simple function of L_{IR} . This implies that a fixed $8\ \mu\text{m}$ to L_{IR} ratio is, to first order, a reasonable assumption for the galaxies in our sample.
- The redshift range over which the F1800W and/or F2100W filters cover the rest-frame $8\ \mu\text{m}$ is $0.9 \lesssim z \lesssim 2$. As such, we test extending our main MIRI-based SFR calibration into the rest-frame $6\ \mu\text{m}$ region, dominated by the weaker 6.2PAH, using the F1280W and F1500W filters. We find that the rest-frame 6 and $8\ \mu\text{m}$ emission display the same behavior and conclude that MIRI photometry covering the rest-frame $6\ \mu\text{m}$ can be used as a robust SFR proxy. This expands the range of our SFR calibrations up to $z \sim 2.8$.
- Finally, we construct composite $\text{UV}+L_{\text{IR}}$ SFR indicators (Eqn 9, Table 3), using the typical formulation which assumes energy balance (Kennicutt et al. 2009; Kennicutt & Evans 2012). The relation between our $\text{UV}+L_{\text{IR}}$ calibration and $\text{SFR}_{\text{Pa}\alpha}$ is well described by a unity slope and tight scatter (~ 0.15 dex). This indicates that the assumption of energy balance holds over our full sample, despite the steep decline in the mid-IR emission.

From the above, we deduce that the mid-IR closely tracks the (global) dust obscuration fraction and thus the obscured

SFR component. The obscuration is known to be a strong function of stellar mass and to have only weak to no evolution with redshift up to $z \sim 3$ (e.g., Whitaker et al. 2017). The implications are: 1) the rest-frame 6 and $8\ \mu\text{m}$ emission, dominated by PAHs, does not significantly change relative to L_{IR} over the mass and metallicity range of our sample. 2) The breakpoint in the mid-IR behavior at $\sim 8 M_{\odot} \text{ yr}^{-1}$ is more fundamentally linked to stellar mass through its relation to the obscured fraction. At this redshift, $8 M_{\odot} \text{ yr}^{-1}$ corresponds to $\log M_{*}/M_{\odot} = 10.1$ for MS galaxies (Leja et al. 2019b). 3) Though our sample only spans $1 < z < 1.75$, the lack of significant redshift evolution of f_{obs} implies that our MIRI-based SFR calibrations and the breakpoint in the mid-IR behavior are valid up to $z \sim 3$, above which the MIRI bands are not longer dominated by dust emission.

Lastly, in Section 7 we extended our analysis to the high luminosity regime of ULIRGs. We compare the behavior of the $7.7\ \mu\text{m}$ PAH vs L_{IR} between local and $z > 0.7$ galaxies, confirming that the PAH deficits seen locally in ULIRGs are not evident at $z > 0.7$ (e.g. Shipley et al. 2016), with the caveat that current samples of high- z ULIRGs show significant scatter. New JWST spectroscopy in four local ULIRGs further reveals that $\text{Pa}\alpha$ in heavily obscured galaxies underestimates the IR-based SFR. This is likely due to dust absorption of ionizing photons in extreme ISM conditions.

1 Acknowledgments: The authors thank Andras Gáspár for his
 2 work on the empirical MIRI PSFs used in extracting pho-
 3 tometry for this work. SA, GHR, and JL acknowledge sup-
 4 port from the JWST Mid-Infrared Instrument (MIRI) Sci-
 5 ence Team Lead, grant 80NSSC18K0555, from NASA God-
 6 dard Space Flight Center to the University of Arizona. ZJ,
 7 JMH, and CNAW acknowledge support from the NIRCам
 8 Science Team contract to the University of Arizona, NAS5-
 9 02105. The research of CCW is supported by NOIRLab,
 10 which is managed by the Association of Universities for Re-
 11 search in Astronomy (AURA) under a cooperative agreement
 12 with the National Science Foundation. IS acknowledges
 13 funding from the European Research Council (ERC) Dis-
 14 tantDust (Grant No.101117541) and the Atracción de Talento
 15 Grant No.2022-T1/TIC-20472 of the Comunidad de Madrid,
 16 Spain. This work is based on observations made with the
 17 NASA/ESA/CSA James Webb Space Telescope. The data
 18 were obtained from the Mikulski Archive for Space Tele-
 19 scopes at the Space Telescope Science Institute, which is
 20 operated by the Association of Universities for Research in
 21 Astronomy, Inc., under NASA contract NAS 5-03127 for
 22 JWST.

Facilities: JWST, HST

Software: JWST Calibration Pipeline (Bushouse et al. 2023), astropy (Astropy Collaboration et al. 2013, 2018, 2022), photutils (Bradley et al. 2025), sep (Bertin & Arnouts

REFERENCES

- Alberts, S., Rujopakarn, W., Rieke, G. H., Jagannathan, P., & Nyland, K. 2020, *ApJ*, 901, 168, doi: [10.3847/1538-4357/abb1a0](https://doi.org/10.3847/1538-4357/abb1a0)
- Alberts, S., Lyu, J., Shivaee, I., et al. 2024, *ApJ*, 976, 224, doi: [10.3847/1538-4357/ad7396](https://doi.org/10.3847/1538-4357/ad7396)
- Alonso-Herrero, A., Rieke, G. H., Rieke, M. J., et al. 2006, *ApJ*, 650, 835, doi: [10.1086/506958](https://doi.org/10.1086/506958)
- Alonso-Herrero, A., Takagi, T., Baker, A. J., et al. 2004, *ApJ*, 612, 222, doi: [10.1086/422448](https://doi.org/10.1086/422448)
- Aniano, G., Draine, B. T., Hunt, L. K., et al. 2020, *ApJ*, 889, 150, doi: [10.3847/1538-4357/ab5fdb](https://doi.org/10.3847/1538-4357/ab5fdb)
- Armus, L., Charmandaris, V., Bernard-Salas, J., et al. 2007, *ApJ*, 656, 148, doi: [10.1086/510107](https://doi.org/10.1086/510107)
- Astropy Collaboration, Robitaille, T. P., Tollerud, E. J., et al. 2013, *A&A*, 558, A33, doi: [10.1051/0004-6361/201322068](https://doi.org/10.1051/0004-6361/201322068)
- Astropy Collaboration, Price-Whelan, A. M., Sipőcz, B. M., et al. 2018, *AJ*, 156, 123, doi: [10.3847/1538-3881/aabc4f](https://doi.org/10.3847/1538-3881/aabc4f)
- Astropy Collaboration, Price-Whelan, A. M., Lim, P. L., et al. 2022, *ApJ*, 935, 167, doi: [10.3847/1538-4357/ac7c74](https://doi.org/10.3847/1538-4357/ac7c74)
- Atek, H., Furtak, L. J., Oesch, P., et al. 2022, *MNRAS*, 511, 4464, doi: [10.1093/mnras/stac360](https://doi.org/10.1093/mnras/stac360)
- Bacon, R., Brinchmann, J., Conseil, S., et al. 2023, *A&A*, 670, A4, doi: [10.1051/0004-6361/202244187](https://doi.org/10.1051/0004-6361/202244187)
- Bakes, E. L. O., & Tielens, A. G. G. M. 1994, *ApJ*, 427, 822, doi: [10.1086/174188](https://doi.org/10.1086/174188)
- Barbary, K. 2016, *Journal of Open Source Software*, 1, 58, doi: [10.21105/joss.00058](https://doi.org/10.21105/joss.00058)
- Baron, D., Sandstrom, K. M., Sutter, J., et al. 2025, *ApJ*, 978, 135, doi: [10.3847/1538-4357/ad972a](https://doi.org/10.3847/1538-4357/ad972a)
- Barrera, N. F., Fuentealba, P., Muñoz, F., Gómez, T., & Cárdenas, C. 2023, *MNRAS*, 524, 3741, doi: [10.1093/mnras/stad2106](https://doi.org/10.1093/mnras/stad2106)
- Bauschlicher, Jr., C. W. 1998, *ApJ*, 509, L125, doi: [10.1086/311782](https://doi.org/10.1086/311782)
- Bell, E. F., Papovich, C., Wolf, C., et al. 2005, *ApJ*, 625, 23, doi: [10.1086/429552](https://doi.org/10.1086/429552)
- Bertin, E., & Arnouts, S. 1996, *A&AS*, 117, 393, doi: [10.1051/aas:1996164](https://doi.org/10.1051/aas:1996164)
- Bian, F., Kewley, L. J., & Dopita, M. A. 2018, *ApJ*, 859, 175, doi: [10.3847/1538-4357/aabd74](https://doi.org/10.3847/1538-4357/aabd74)
- Böker, T., Beck, T. L., Birkmann, S. M., et al. 2023, *PASP*, 135, 038001, doi: [10.1088/1538-3873/acb846](https://doi.org/10.1088/1538-3873/acb846)
- Boquien, M., & Salim, S. 2021, *A&A*, 653, A149, doi: [10.1051/0004-6361/202140992](https://doi.org/10.1051/0004-6361/202140992)
- Bouwens, R. J., Aravena, M., Decarli, R., et al. 2016, *ApJ*, 833, 72, doi: [10.3847/1538-4357/833/1/72](https://doi.org/10.3847/1538-4357/833/1/72)
- Bradley, L., Sipőcz, B., Robitaille, T., et al. 2025, doi: [10.5281/zenodo.14889440](https://doi.org/10.5281/zenodo.14889440)
- Brammer, G., & Matharu, J. 2021, Zenodo, doi: [10.5281/zenodo.5012699](https://doi.org/10.5281/zenodo.5012699)
- Bunker, A. J., Cameron, A. J., Curtis-Lake, E., et al. 2024, *A&A*, 690, A288, doi: [10.1051/0004-6361/202347094](https://doi.org/10.1051/0004-6361/202347094)
- Bushouse, H., Eisenhamer, J., Dencheva, N., et al. 2023, Zenodo, doi: [10.5281/zenodo.10022973](https://doi.org/10.5281/zenodo.10022973)
- Byler, N., Dalcanton, J. J., Conroy, C., & Johnson, B. D. 2017, *ApJ*, 840, 44, doi: [10.3847/1538-4357/aa6c66](https://doi.org/10.3847/1538-4357/aa6c66)
- Calapa, M. D., Calzetti, D., Draine, B. T., et al. 2014, *ApJ*, 784, 130, doi: [10.1088/0004-637X/784/2/130](https://doi.org/10.1088/0004-637X/784/2/130)
- Calzetti, D. 2013, in *Secular Evolution of Galaxies*, 419, doi: [10.48550/arXiv.1208.2997](https://doi.org/10.48550/arXiv.1208.2997)
- Calzetti, D., Armus, L., Bohlin, R. C., et al. 2000, *ApJ*, 533, 682, doi: [10.1086/308692](https://doi.org/10.1086/308692)
- Calzetti, D., Kennicutt, R. C., Engelbracht, C. W., et al. 2007, *ApJ*, 666, 870, doi: [10.1086/520082](https://doi.org/10.1086/520082)
- Calzetti, D., Wu, S. Y., Hong, S., et al. 2010, *ApJ*, 714, 1256, doi: [10.1088/0004-637X/714/2/1256](https://doi.org/10.1088/0004-637X/714/2/1256)
- Calzetti, D., Kennicutt, R. C., Adamo, A., et al. 2025, *ApJ*, 991, 198, doi: [10.3847/1538-4357/adfbc0](https://doi.org/10.3847/1538-4357/adfbc0)
- Cardelli, J. A., Clayton, G. C., & Mathis, J. S. 1989, *ApJ*, 345, 245, doi: [10.1086/167900](https://doi.org/10.1086/167900)
- Charlot, S., & Fall, S. M. 2000, *ApJ*, 539, 718, doi: [10.1086/309250](https://doi.org/10.1086/309250)
- Chasteney, J., Sandstrom, K., Chiang, I.-D., et al. 2019, *ApJ*, 876, 62, doi: [10.3847/1538-4357/ab16cf](https://doi.org/10.3847/1538-4357/ab16cf)
- Chasteney, J., Sandstrom, K., Leroy, A. K., et al. 2025, *ApJSuppl. Ser.*, 276, 2, doi: [10.3847/1538-4365/ad8a5c](https://doi.org/10.3847/1538-4365/ad8a5c)
- Chisholm, J., Rigby, J. R., Bayliss, M., et al. 2019, *ApJ*, 882, 182, doi: [10.3847/1538-4357/ab3104](https://doi.org/10.3847/1538-4357/ab3104)
- Cleri, N. J., Trump, J. R., Backhaus, B. E., et al. 2022, *ApJ*, 929, 3, doi: [10.3847/1538-4357/ac5a4c](https://doi.org/10.3847/1538-4357/ac5a4c)
- Cluver, M. E., Jarrett, T. H., Dale, D. A., et al. 2017, *ApJ*, 850, 68, doi: [10.3847/1538-4357/aa92c7](https://doi.org/10.3847/1538-4357/aa92c7)
- Conroy, C., & Gunn, J. E. 2010, *ApJ*, 712, 833, doi: [10.1088/0004-637X/712/2/833](https://doi.org/10.1088/0004-637X/712/2/833)
- Conroy, C., Gunn, J. E., & White, M. 2009, *ApJ*, 699, 486, doi: [10.1088/0004-637X/699/1/486](https://doi.org/10.1088/0004-637X/699/1/486)
- Crocker, A. F., Calzetti, D., Thilker, D. A., et al. 2013, *ApJ*, 762, 79, doi: [10.1088/0004-637X/762/2/79](https://doi.org/10.1088/0004-637X/762/2/79)
- Dale, D. A., & Helou, G. 2002, *ApJ*, 576, 159, doi: [10.1086/341632](https://doi.org/10.1086/341632)
- Dannerbauer, H., Rigopoulou, D., Lutz, D., et al. 2005, *A&A*, 441, 999, doi: [10.1051/0004-6361:20052812](https://doi.org/10.1051/0004-6361:20052812)

- Dasyra, K. M., Yan, L., Helou, G., et al. 2009, *ApJ*, 701, 1123, doi: [10.1088/0004-637X/701/2/1123](https://doi.org/10.1088/0004-637X/701/2/1123)
- De Rossi, M. E., Rieke, G. H., Shivaeei, I., Bromm, V., & Lyu, J. 2018, *ApJ*, 869, 4, doi: [10.3847/1538-4357/aaebf8](https://doi.org/10.3847/1538-4357/aaebf8)
- D'Eugenio, F., Cameron, A. J., Scholtz, J., et al. 2025, *ApJS*, 277, 4, doi: [10.3847/1538-4365/ada148](https://doi.org/10.3847/1538-4365/ada148)
- Diamond-Stanic, A. M., & Rieke, G. H. 2010, *ApJ*, 724, 140, doi: [10.1088/0004-637X/724/1/140](https://doi.org/10.1088/0004-637X/724/1/140)
- Díaz-Santos, T., Alonso-Herrero, A., Colina, L., et al. 2008, *ApJ*, 685, 211, doi: [10.1086/588276](https://doi.org/10.1086/588276)
- Dole, H., Rieke, G. H., Lagache, G., et al. 2004, *ApJS*, 154, 93, doi: [10.1086/422690](https://doi.org/10.1086/422690)
- Dole, H., Lagache, G., Puget, J.-L., et al. 2006, *A&A*, 451, 417, doi: [10.1051/0004-6361:20054446](https://doi.org/10.1051/0004-6361:20054446)
- Domínguez, A., Siana, B., Brooks, A. M., et al. 2015, *MNRAS*, 451, 839, doi: [10.1093/mnras/stv1001](https://doi.org/10.1093/mnras/stv1001)
- Donnan, F. R., García-Bernete, I., Rigopoulou, D., et al. 2024, *MNRAS*, 529, 1386, doi: [10.1093/mnras/stae612](https://doi.org/10.1093/mnras/stae612)
- Dopita, M. A., Groves, B. A., Sutherland, R. S., & Kewley, L. J. 2003, *ApJ*, 583, 727, doi: [10.1086/345448](https://doi.org/10.1086/345448)
- Draine, B. T., & Li, A. 2007, *ApJ*, 657, 810, doi: [10.1086/511055](https://doi.org/10.1086/511055)
- Draine, B. T., Li, A., Hensley, B. S., et al. 2021, *ApJ*, 917, 3, doi: [10.3847/1538-4357/abff51](https://doi.org/10.3847/1538-4357/abff51)
- Egorov, O. V., Kreckel, K., Sandstrom, K. M., et al. 2023, *ApJ*, 944, L16, doi: [10.3847/2041-8213/acac92](https://doi.org/10.3847/2041-8213/acac92)
- Egorov, O. V., Leroy, A. K., Sandstrom, K., et al. 2025, *A&A*, 703, A103, doi: [10.1051/0004-6361/202556427](https://doi.org/10.1051/0004-6361/202556427)
- Eisenstein, D. J., Willott, C., Alberts, S., et al. 2026, *ApJS*, 283, 6, doi: [10.3847/1538-4365/ae3163](https://doi.org/10.3847/1538-4365/ae3163)
- Elbaz, D., Le Flocc'h, E., Dole, H., & Marcillac, D. 2005, *A&A*, 434, L1, doi: [10.1051/0004-6361:200500095](https://doi.org/10.1051/0004-6361:200500095)
- Elbaz, D., Hwang, H. S., Magnelli, B., et al. 2010, *A&A*, 518, L29, doi: [10.1051/0004-6361/201014687](https://doi.org/10.1051/0004-6361/201014687)
- Elbaz, D., Dickinson, M., Hwang, H. S., et al. 2011, *A&A*, 533, A119, doi: [10.1051/0004-6361/201117239](https://doi.org/10.1051/0004-6361/201117239)
- Emami, N., Siana, B., Weisz, D. R., et al. 2019, *ApJ*, 881, 71, doi: [10.3847/1538-4357/ab211a](https://doi.org/10.3847/1538-4357/ab211a)
- Engelbracht, C. W., Gordon, K. D., Rieke, G. H., et al. 2005, *ApJ*, 628, L29, doi: [10.1086/432613](https://doi.org/10.1086/432613)
- Engelbracht, C. W., Rieke, G. H., Gordon, K. D., et al. 2008, *ApJ*, 678, 804, doi: [10.1086/529513](https://doi.org/10.1086/529513)
- Farrah, D., Bernard-Salas, J., Spoon, H. W. W., et al. 2007, *ApJ*, 667, 149, doi: [10.1086/520834](https://doi.org/10.1086/520834)
- Fiolet, N., Omont, A., Lagache, G., et al. 2010, *A&A*, 524, A33, doi: [10.1051/0004-6361/201015504](https://doi.org/10.1051/0004-6361/201015504)
- Flores Velázquez, J. A., Gurvich, A. B., Faucher-Giguère, C.-A., et al. 2021, *MNRAS*, 501, 4812, doi: [10.1093/mnras/staa3893](https://doi.org/10.1093/mnras/staa3893)
- Florian, M. K., Rieke, G. H., Alberts, S., et al. 2025, *ApJ*, 990, 102, doi: [10.3847/1538-4357/adee1d](https://doi.org/10.3847/1538-4357/adee1d)
- Foley, N., Cazaux, S., Egorov, D., et al. 2018, *MNRAS*, 479, 649, doi: [10.1093/mnras/sty1528](https://doi.org/10.1093/mnras/sty1528)
- Fumagalli, M., Labbé, I., Patel, S. G., et al. 2014, *ApJ*, 796, 35, doi: [10.1088/0004-637X/796/1/35](https://doi.org/10.1088/0004-637X/796/1/35)
- Galliano, F., Dwek, E., & Chantal, P. 2008, *ApJ*, 672, 214, doi: [10.1086/523621](https://doi.org/10.1086/523621)
- García-Bernete, I., Rigopoulou, D., Alonso-Herrero, A., et al. 2022, *A&A*, 666, L5, doi: [10.1051/0004-6361/202244806](https://doi.org/10.1051/0004-6361/202244806)
- Gardner, J. P., Mather, J. C., Abbott, R., et al. 2023, *PASP*, 135, 068001, doi: [10.1088/1538-3873/acd1b5](https://doi.org/10.1088/1538-3873/acd1b5)
- Giménez-Arteaga, C., Brammer, G. B., Marchesini, D., et al. 2022, *ApJ Suppl. Ser.*, 263, 17, doi: [10.3847/1538-4365/ac958c](https://doi.org/10.3847/1538-4365/ac958c)
- Goldberg, C. E., Buiten, V. A., Rieke, G. H., et al. 2024, *ApJ*, 977, 55, doi: [10.3847/1538-4357/ad7eb0](https://doi.org/10.3847/1538-4357/ad7eb0)
- Gordon, K. D., Calzetti, D., & Witt, A. N. 1997, *ApJ*, 487, 625, doi: [10.1086/304654](https://doi.org/10.1086/304654)
- Gordon, K. D., Misselt, K. A., Bouwman, J., et al. 2021, *ApJ*, 916, 33, doi: [10.3847/1538-4357/ac00b7](https://doi.org/10.3847/1538-4357/ac00b7)
- Gordon, K. D., Fitzpatrick, E. L., Massa, D., et al. 2024, *ApJ*, 970, 51, doi: [10.3847/1538-4357/ad4be1](https://doi.org/10.3847/1538-4357/ad4be1)
- Guo, Y., Rafelski, M., Faber, S. M., et al. 2016, *ApJ*, 833, 37, doi: [10.3847/1538-4357/833/1/37](https://doi.org/10.3847/1538-4357/833/1/37)
- Hao, C.-N., Kennicutt, R. C., Johnson, B. D., et al. 2011, *ApJ*, 741, 124, doi: [10.1088/0004-637X/741/2/124](https://doi.org/10.1088/0004-637X/741/2/124)
- Hayward, C. C., Lanz, L., Ashby, M. L. N., et al. 2014, *MNRAS*, 445, 1598, doi: [10.1093/mnras/stu1843](https://doi.org/10.1093/mnras/stu1843)
- Helou, G., Malhotra, S., Hollenbach, D. J., Dale, D. A., & Contursi, A. 2001, *ApJ*, 548, L73, doi: [10.1086/318916](https://doi.org/10.1086/318916)
- Huang, J. S., Faber, S. M., Daddi, E., et al. 2009, *ApJ*, 700, 183, doi: [10.1088/0004-637X/700/1/183](https://doi.org/10.1088/0004-637X/700/1/183)
- Hummer, D. G., & Storey, P. J. 1987, *MNRAS*, 224, 801, doi: [10.1093/mnras/224.3.801](https://doi.org/10.1093/mnras/224.3.801)
- Hunt, L. K., Thuan, T. X., Izotov, Y. I., & Sauvage, M. 2010, *ApJ*, 712, 164, doi: [10.1088/0004-637X/712/1/164](https://doi.org/10.1088/0004-637X/712/1/164)
- Hunter, J. D. 2007, *Computing in Science & Engineering*, 9, 90, doi: [10.1109/MCSE.2007.55](https://doi.org/10.1109/MCSE.2007.55)
- Illingworth, G., Magee, D., Bouwens, R., et al. 2016, *The Hubble Legacy Fields (HLF-GOODS-S) v1.5 Data Products: Combining 2442 Orbits of GOODS-S/CDF-S Region ACS and WFC3/IR Images*, doi: [10.48550/arXiv.1606.00841](https://doi.org/10.48550/arXiv.1606.00841)
- Inami, H., Armus, L., Matsuhara, H., et al. 2018, *A&A*, 617, A130, doi: [10.1051/0004-6361/201833053](https://doi.org/10.1051/0004-6361/201833053)
- Inoue, A. K., Hirashita, H., & Kamaya, H. 2001, *ApJ*, 555, 613, doi: [10.1086/321499](https://doi.org/10.1086/321499)
- Jakobsen, P., Ferruit, P., Alves de Oliveira, C., et al. 2022, *A&A*, 661, A80, doi: [10.1051/0004-6361/202142663](https://doi.org/10.1051/0004-6361/202142663)
- Ji, Z., Williams, C. C., Tacchella, S., et al. 2023, *JADES + JEMS: A Detailed Look at the Buildup of Central Stellar Cores and Suppression of Star Formation in Galaxies at Redshifts $3 < z < 4.5$* , doi: [10.48550/arXiv.2305.18518](https://doi.org/10.48550/arXiv.2305.18518)

- Johnson, B. D., Leja, J., Conroy, C., & Speagle, J. S. 2021, *ApJ Suppl. Ser.*, 254, 22, doi: [10.3847/1538-4365/abef67](https://doi.org/10.3847/1538-4365/abef67)
- Kennicutt, R. C., & Evans, N. J. 2012, *Annu. Rev. A&A* Vol 50 P531-608, 50, 531, doi: [10.1146/annurev-astro-081811-125610](https://doi.org/10.1146/annurev-astro-081811-125610)
- Kennicutt, Jr., R. C., Calzetti, D., Walter, F., et al. 2007, *ApJ*, 671, 333, doi: [10.1086/522300](https://doi.org/10.1086/522300)
- Kennicutt, Jr., R. C., Hao, C.-N., Calzetti, D., et al. 2009, *ApJ*, 703, 1672, doi: [10.1088/0004-637X/703/2/1672](https://doi.org/10.1088/0004-637X/703/2/1672)
- Kessler, M. F., Steinz, J. A., Anderegg, M. E., et al. 1996, *A&A*, 315, L27
- Kim, H. K., Malkan, M. A., Takagi, T., et al. 2024, *ApJ*, 974, 253, doi: [10.3847/1538-4357/ad72e6](https://doi.org/10.3847/1538-4357/ad72e6)
- Kirkpatrick, A., Pope, A., Sajina, A., et al. 2015, *ApJ*, 814, 9, doi: [10.1088/0004-637X/814/1/9](https://doi.org/10.1088/0004-637X/814/1/9)
- Kirkpatrick, A., Yang, G., Bail, A. L., et al. 2023, CEERS Key Paper VII: JWST/MIRI Reveals a Faint Population of Galaxies at Cosmic Noon Unseen by Spitzer, arXiv, doi: [10.48550/arXiv.2308.09750](https://doi.org/10.48550/arXiv.2308.09750)
- Kodra, D., Andrews, B. H., Newman, J. A., et al. 2023, *ApJ*, 942, 36, doi: [10.3847/1538-4357/ac9f12](https://doi.org/10.3847/1538-4357/ac9f12)
- Kovács, T. O., Burgarella, D., Kaneda, H., et al. 2019, *PASJ*, 71, 27, doi: [10.1093/pasj/psy145](https://doi.org/10.1093/pasj/psy145)
- Kriek, M., & Conroy, C. 2013, *ApJ*, 775, L16, doi: [10.1088/2041-8205/775/1/L16](https://doi.org/10.1088/2041-8205/775/1/L16)
- Kron, R. G. 1980, *ApJ Suppl. Ser.*, 43, 305, doi: [10.1086/190669](https://doi.org/10.1086/190669)
- Lagache, G., Puget, J.-L., & Dole, H. 2005, *ARA&A*, 43, 727, doi: [10.1146/annurev.astro.43.072103.150606](https://doi.org/10.1146/annurev.astro.43.072103.150606)
- Lai, T. S.-Y., Smith, J. D. T., Baba, S., Spoon, H. W. W., & Imanishi, M. 2020, *ApJ*, 905, 55, doi: [10.3847/1538-4357/abc002](https://doi.org/10.3847/1538-4357/abc002)
- Lai, T. S.-Y., Armus, L., U, V., et al. 2022, *ApJL*, 941, L36, doi: [10.3847/2041-8213/ac9ebf](https://doi.org/10.3847/2041-8213/ac9ebf)
- Le Flocc'h, E., Papovich, C., Dole, H., et al. 2005, *ApJ*, 632, 169, doi: [10.1086/432789](https://doi.org/10.1086/432789)
- Lee, N., Sanders, D. B., Casey, C. M., et al. 2015, *ApJ*, 801, 80, doi: [10.1088/0004-637X/801/2/80](https://doi.org/10.1088/0004-637X/801/2/80)
- Leitherer, C. 1990, *ApJS*, 73, 1, doi: [10.1086/191438](https://doi.org/10.1086/191438)
- Leja, J., Carnall, A. C., Johnson, B. D., Conroy, C., & Speagle, J. S. 2019a, *ApJ*, 876, 3, doi: [10.3847/1538-4357/ab133c](https://doi.org/10.3847/1538-4357/ab133c)
- Leja, J., Johnson, B. D., Conroy, C., et al. 2019b, *ApJ*, 877, 140, doi: [10.3847/1538-4357/ab1d5a](https://doi.org/10.3847/1538-4357/ab1d5a)
- Leja, J., Speagle, J. S., Ting, Y.-S., et al. 2022, *ApJ*, 936, 165, doi: [10.3847/1538-4357/ac887d](https://doi.org/10.3847/1538-4357/ac887d)
- Leroy, A. K., Bolatto, A. D., Sandstrom, K., et al. 2023, *ApJL*, 944, L10, doi: [10.3847/2041-8213/acab01](https://doi.org/10.3847/2041-8213/acab01)
- Li, A. 2020, *Nat. Astron.*, 4, 339, doi: [10.1038/s41550-020-1051-1](https://doi.org/10.1038/s41550-020-1051-1)
- Liang, L., Feldmann, R., Hayward, C. C., et al. 2021, *MNRAS*, 502, 3210, doi: [10.1093/mnras/stab096](https://doi.org/10.1093/mnras/stab096)
- Lorenz, B., Suess, K. A., Kriek, M., et al. 2025, *ApJ*, 988, L20, doi: [10.3847/2041-8213/ade887](https://doi.org/10.3847/2041-8213/ade887)
- Lyu, J., Alberts, S., Rieke, G. H., & Rujopakarn, W. 2022, *ApJ*, 941, 191, doi: [10.3847/1538-4357/ac9e5d](https://doi.org/10.3847/1538-4357/ac9e5d)
- Lyu, J., Yang, X., Li, A., et al. 2025, Unveiling the Aromatic and Aliphatic Universe at Redshifts $z \sim 0.2-0.5$ with JWST/NIRCam, arXiv, doi: [10.48550/arXiv.2502.18464](https://doi.org/10.48550/arXiv.2502.18464)
- Lyu, J., Alberts, S., Rieke, G. H., et al. 2024, *ApJ*, 966, 229, doi: [10.3847/1538-4357/ad3643](https://doi.org/10.3847/1538-4357/ad3643)
- Madau, P., & Dickinson, M. 2014, *Annu. Rev. A&A*, 52, 415, doi: [10.1146/annurev-astro-081811-125615](https://doi.org/10.1146/annurev-astro-081811-125615)
- Madden, S. C., Galliano, F., Jones, A. P., & Sauvage, M. 2006, *A&A*, 446, 877, doi: [10.1051/0004-6361:20053890](https://doi.org/10.1051/0004-6361:20053890)
- Magdis, G. E., Daddi, E., Béthermin, M., et al. 2012, *ApJ*, 760, 6, doi: [10.1088/0004-637X/760/1/6](https://doi.org/10.1088/0004-637X/760/1/6)
- Magdis, G. E., Rigopoulou, D., Helou, G., et al. 2013, *A&A*, 558, A136, doi: [10.1051/0004-6361/201322226](https://doi.org/10.1051/0004-6361/201322226)
- Magnelli, B., Elbaz, D., Chary, R. R., et al. 2011, *A&A*, 528, A35, doi: [10.1051/0004-6361/200913941](https://doi.org/10.1051/0004-6361/200913941)
- Mahajan, S., Ashby, M. L. N., Willner, S. P., et al. 2019, *MNRAS*, 482, 560, doi: [10.1093/mnras/sty2699](https://doi.org/10.1093/mnras/sty2699)
- Maiolino, R., & Mannucci, F. 2019, *A&A Rev.*, 27, 3, doi: [10.1007/s00159-018-0112-2](https://doi.org/10.1007/s00159-018-0112-2)
- Marble, A. R., Engelbracht, C. W., van Zee, L., et al. 2010, *ApJ*, 715, 506, doi: [10.1088/0004-637X/715/1/506](https://doi.org/10.1088/0004-637X/715/1/506)
- McKinney, J., Eleazer, M., Pope, A., et al. 2025, A JWST MIRI LRS Survey of 37 Massive Star-Forming Galaxies and AGN at Cosmic Noon – Overview and First Results, arXiv, doi: [10.48550/arXiv.2510.07365](https://doi.org/10.48550/arXiv.2510.07365)
- McLure, R. J., Dunlop, J. S., Cullen, F., et al. 2018, *MNRAS*, 476, 3991, doi: [10.1093/mnras/sty522](https://doi.org/10.1093/mnras/sty522)
- McNulty, S., Song, M., Whitaker, K. E., et al. 2026, 3D-Herschel: Constraining Dust Emission with Panchromatic Modeling of 3D-HST Galaxies, arXiv, doi: [10.48550/arXiv.2602.22384](https://doi.org/10.48550/arXiv.2602.22384)
- Murphy, E. J., Condon, J. J., Schinnerer, E., et al. 2011, *ApJ*, 737, 67, doi: [10.1088/0004-637X/737/2/67](https://doi.org/10.1088/0004-637X/737/2/67)
- Murphy, Jr., T. W., Soifer, B. T., Matthews, K., Armus, L., & Kiger, J. R. 2001, *Astron. J.*, 121, 97, doi: [10.1086/318031](https://doi.org/10.1086/318031)
- Muzzin, A., Suess, K. A., Marchesini, D., et al. 2025, MINERVA: A NIRCam Medium Band and MIRI Imaging Survey to Unlock the Hidden Gems of the Distant Universe, arXiv, doi: [10.48550/arXiv.2507.19706](https://doi.org/10.48550/arXiv.2507.19706)
- Narayanan, D., Davé, R., Johnson, B. D., et al. 2018, *MNRAS*, 474, 1718, doi: [10.1093/mnras/stx2860](https://doi.org/10.1093/mnras/stx2860)
- Navarro-Carrera, R., Rinaldi, P., Caputi, K. I., et al. 2026, *ApJ*, 996, 70, doi: [10.3847/1538-4357/ae1609](https://doi.org/10.3847/1538-4357/ae1609)
- Neufeld, C., van Dokkum, P., Asali, Y., et al. 2024, FRESCO: The Paschen- α Star Forming Sequence at Cosmic Noon, doi: [10.48550/arXiv.2404.10816](https://doi.org/10.48550/arXiv.2404.10816)
- Noll, S., Burgarella, D., Giovannoli, E., et al. 2009, *A&A*, 507, 1793, doi: [10.1051/0004-6361/200912497](https://doi.org/10.1051/0004-6361/200912497)

- Oesch, P. A., Brammer, G., Naidu, R. P., et al. 2023, The JWST FRESCO Survey: Legacy NIRCcam/Grism Spectroscopy and Imaging in the Two GOODS Fields, arXiv, <https://arxiv.org/abs/2304.02026>
- Oke, J. B., & Gunn, J. E. 1983, *ApJ*, 266, 713, doi: [10.1086/160817](https://doi.org/10.1086/160817)
- Osterbrock, D. E. 1989, *Ann. N. Y. Acad. Sci.*, 571, 99, doi: [10.1111/j.1749-6632.1989.tb50500.x](https://doi.org/10.1111/j.1749-6632.1989.tb50500.x)
- Papovich, C., Rudnick, G., Le Floch, E., et al. 2007, *ApJ*, 668, 45, doi: [10.1086/521090](https://doi.org/10.1086/521090)
- Pedrini, A., Adamo, A., Calzetti, D., et al. 2024, *ApJ*, 971, 32, doi: [10.3847/1538-4357/ad534d](https://doi.org/10.3847/1538-4357/ad534d)
- Perna, M., Arribas, S., Lamperti, I., et al. 2024, *A&A*, 690, A171, doi: [10.1051/0004-6361/202450094](https://doi.org/10.1051/0004-6361/202450094)
- Pilbratt, G. L., Riedinger, J. R., Passvogel, T., et al. 2010, *A&A*, 518, L1, doi: [10.1051/0004-6361/201014759](https://doi.org/10.1051/0004-6361/201014759)
- Planck Collaboration, Aghanim, N., Akrami, Y., et al. 2020, *A&A*, 641, A1, doi: [10.1051/0004-6361/201833880](https://doi.org/10.1051/0004-6361/201833880)
- Pope, A., Chary, R.-R., Alexander, D. M., et al. 2008, *ApJ*, 675, 1171, doi: [10.1086/527030](https://doi.org/10.1086/527030)
- Pope, A., Wagg, J., Frayer, D., et al. 2013, *ApJ*, 772, 92, doi: [10.1088/0004-637X/772/2/92](https://doi.org/10.1088/0004-637X/772/2/92)
- Popesso, P., Concas, A., Cresci, G., et al. 2023, *MNRAS*, 519, 1526, doi: [10.1093/mnras/stac3214](https://doi.org/10.1093/mnras/stac3214)
- Popping, G., & Péroux, C. 2022, *Monthly Notices of the Royal Astronomical Society*, 513, 1531, doi: [10.1093/mnras/stac695](https://doi.org/10.1093/mnras/stac695)
- Popping, G., Somerville, R. S., & Galametz, M. 2017, *MNRAS*, 471, 3152, doi: [10.1093/mnras/stx1545](https://doi.org/10.1093/mnras/stx1545)
- Reddy, N., Dickinson, M., Elbaz, D., et al. 2012, *ApJ*, 744, 154, doi: [10.1088/0004-637X/744/2/154](https://doi.org/10.1088/0004-637X/744/2/154)
- Reddy, N. A., Erb, D. K., Pettini, M., Steidel, C. C., & Shapley, A. E. 2010, *ApJ*, 712, 1070, doi: [10.1088/0004-637X/712/2/1070](https://doi.org/10.1088/0004-637X/712/2/1070)
- Reddy, N. A., Steidel, C. C., Fadda, D., et al. 2006, *ApJ*, 644, 792, doi: [10.1086/503739](https://doi.org/10.1086/503739)
- Reddy, N. A., Steidel, C. C., Pettini, M., et al. 2008, *ApJ Suppl. Ser.*, 175, 48, doi: [10.1086/521105](https://doi.org/10.1086/521105)
- Reddy, N. A., Topping, M. W., Sanders, R. L., Shapley, A. E., & Brammer, G. 2023a, *ApJ*, 948, 83, doi: [10.3847/1538-4357/acc869](https://doi.org/10.3847/1538-4357/acc869)
- Reddy, N. A., Kriek, M., Shapley, A. E., et al. 2015, *ApJ*, 806, 259, doi: [10.1088/0004-637X/806/2/259](https://doi.org/10.1088/0004-637X/806/2/259)
- Reddy, N. A., Oesch, P. A., Bouwens, R. J., et al. 2018, *ApJ*, 853, 56, doi: [10.3847/1538-4357/aaa3e7](https://doi.org/10.3847/1538-4357/aaa3e7)
- Reddy, N. A., Shapley, A. E., Kriek, M., et al. 2020, *ApJ*, 902, 123, doi: [10.3847/1538-4357/abb674](https://doi.org/10.3847/1538-4357/abb674)
- Reddy, N. A., Topping, M. W., Shapley, A. E., et al. 2022, *ApJ*, 926, 31, doi: [10.3847/1538-4357/ac3b4c](https://doi.org/10.3847/1538-4357/ac3b4c)
- Reddy, N. A., Sanders, R. L., Shapley, A. E., et al. 2023b, The Impact of Star-Formation-Rate Surface Density on the Electron Density and Ionization Parameter of High-Redshift Galaxies, doi: [10.48550/arXiv.2302.10213](https://doi.org/10.48550/arXiv.2302.10213)
- Reddy, N. A., Shapley, A. E., Sanders, R. L., et al. 2025, The JWST/AURORA Survey: Multiple Balmer and Paschen Emission Lines for Individual Star-forming Galaxies at $Z=1.5-4.4$. I. A Diversity of Nebular Attenuation Curves and Evidence for Non-Unity Dust Covering Fractions, arXiv, doi: [10.48550/arXiv.2506.17396](https://doi.org/10.48550/arXiv.2506.17396)
- . 2026, *ApJ*, 999, 15, doi: [10.3847/1538-4357/ae38da](https://doi.org/10.3847/1538-4357/ae38da)
- Rémy-Ruyer, A., Madden, S. C., Galliano, F., et al. 2015, *A&A*, 582, A121, doi: [10.1051/0004-6361/201526067](https://doi.org/10.1051/0004-6361/201526067)
- Rieke, G., Albers, S., Shivaei, I., et al. 2024, The SMILES Mid-Infrared Survey, doi: [10.48550/arXiv.2406.03518](https://doi.org/10.48550/arXiv.2406.03518)
- Rieke, G. H., Alonso-Herrero, A., Weiner, B. J., et al. 2009, *ApJ*, 692, 556, doi: [10.1088/0004-637X/692/1/556](https://doi.org/10.1088/0004-637X/692/1/556)
- Rieke, G. H., Young, E. T., Engelbracht, C. W., et al. 2004, *ApJ Suppl. Ser.*, 154, 25, doi: [10.1086/422717](https://doi.org/10.1086/422717)
- Rieke, G. H., Wright, G. S., Böker, T., et al. 2015, *PASP*, 127, 584, doi: [10.1086/682252](https://doi.org/10.1086/682252)
- Rieke, G. H., Buiten, V. A., Goldberg, C. E., et al. 2025, *ApJ*, 988, 17, doi: [10.3847/1538-4357/add2fd](https://doi.org/10.3847/1538-4357/add2fd)
- Rieke, M., & the JADES Collaboration. 2023, JADES Initial Data Release for the Hubble Ultra Deep Field: Revealing the Faint Infrared Sky with Deep JWST NIRCcam Imaging, doi: [10.48550/arXiv.2306.02466](https://doi.org/10.48550/arXiv.2306.02466)
- Rigby, J., Perrin, M., McElwain, M., et al. 2023, *PASP*, 135, 048001, doi: [10.1088/1538-3873/acb293](https://doi.org/10.1088/1538-3873/acb293)
- Rigby, J. R., & Rieke, G. H. 2004, *ApJ*, 606, 237, doi: [10.1086/382776](https://doi.org/10.1086/382776)
- Rigby, J. R., Marcillac, D., Egami, E., et al. 2008, *ApJ*, 675, 262, doi: [10.1086/525273](https://doi.org/10.1086/525273)
- Rodighiero, G., Daddi, E., Baronchelli, I., et al. 2011, *ApJL*, 739, L40, doi: [10.1088/2041-8205/739/2/L40](https://doi.org/10.1088/2041-8205/739/2/L40)
- Ronayne, K., Papovich, C., Yang, G., et al. 2023, CEERS: 7.7 μm PAH Star Formation Rate Calibration with JWST MIRI, arXiv, doi: [10.48550/arXiv.2310.07766](https://doi.org/10.48550/arXiv.2310.07766)
- Rujopakarn, W., Rieke, G. H., Eisenstein, D. J., & Juneau, S. 2011, *ApJ*, 726, 93, doi: [10.1088/0004-637X/726/2/93](https://doi.org/10.1088/0004-637X/726/2/93)
- Rujopakarn, W., Rieke, G. H., Weiner, B. J., et al. 2013, *ApJ*, 767, 73, doi: [10.1088/0004-637X/767/1/73](https://doi.org/10.1088/0004-637X/767/1/73)
- Sajina, A., Yan, L., Armus, L., et al. 2007, *ApJ*, 664, 713, doi: [10.1086/519446](https://doi.org/10.1086/519446)
- Sanders, D. B., Mazzarella, J. M., Kim, D. C., Surace, J. A., & Soifer, B. T. 2003, *Astron. J.*, 126, 1607, doi: [10.1086/376841](https://doi.org/10.1086/376841)
- Sanders, R. L., Shapley, A. E., Zhang, K., & Yan, R. 2017, *ApJ*, 850, 136, doi: [10.3847/1538-4357/aa93e4](https://doi.org/10.3847/1538-4357/aa93e4)
- Sanders, R. L., Shapley, A. E., Jones, T., et al. 2021, *ApJ*, 914, 19, doi: [10.3847/1538-4357/abf4c1](https://doi.org/10.3847/1538-4357/abf4c1)

- Sandstrom, K. M., Bolatto, A. D., Bot, C., et al. 2012, *ApJ*, 744, 20, doi: [10.1088/0004-637X/744/1/20](https://doi.org/10.1088/0004-637X/744/1/20)
- Shapley, A. E., Sanders, R. L., Salim, S., et al. 2022, *ApJ*, 926, 145, doi: [10.3847/1538-4357/ac4742](https://doi.org/10.3847/1538-4357/ac4742)
- Shim, H., Hwang, H. S., Jeong, W.-S., et al. 2023, *Astron. J.*, 165, 31, doi: [10.3847/1538-3881/aca09c](https://doi.org/10.3847/1538-3881/aca09c)
- Shipley, H. V., Papovich, C., Rieke, G. H., Brown, M. J. I., & Moustakas, J. 2016, *ApJ*, 818, 60, doi: [10.3847/0004-637X/818/1/60](https://doi.org/10.3847/0004-637X/818/1/60)
- Shivaei, I., Reddy, N. A., Shapley, A. E., et al. 2017, *ApJ*, 837, 157, doi: [10.3847/1538-4357/aa619c](https://doi.org/10.3847/1538-4357/aa619c)
- Shivaei, I., Reddy, N., Rieke, G., et al. 2020, *ApJ*, 899, 117, doi: [10.3847/1538-4357/aba35e](https://doi.org/10.3847/1538-4357/aba35e)
- Shivaei, I., Alberts, S., Florian, M., et al. 2024, A New Census of Dust and PAHs at $Z=0.7-2$ with JWST MIRI, doi: [10.48550/arXiv.2402.07989](https://doi.org/10.48550/arXiv.2402.07989)
- Siana, B., Teplitz, H. I., Chary, R.-R., Colbert, J., & Frayer, D. T. 2008, *ApJ*, 689, 59, doi: [10.1086/592682](https://doi.org/10.1086/592682)
- Siana, B., Smail, I., Swinbank, A. M., et al. 2009, *ApJ*, 698, 1273, doi: [10.1088/0004-637X/698/2/1273](https://doi.org/10.1088/0004-637X/698/2/1273)
- Simons, R. C., Papovich, C., Momcheva, I. G., et al. 2023, *ApJSuppl. Ser.*, 266, 13, doi: [10.3847/1538-4365/acc517](https://doi.org/10.3847/1538-4365/acc517)
- Smith, J. D. T., Draine, B. T., Dale, D. A., et al. 2007, *ApJ*, 656, 770, doi: [10.1086/510549](https://doi.org/10.1086/510549)
- Spilker, J. S., Marrone, D. P., Aravena, M., et al. 2016, *ApJ*, 826, 112, doi: [10.3847/0004-637X/826/2/112](https://doi.org/10.3847/0004-637X/826/2/112)
- Steidel, C. C., Strom, A. L., Pettini, M., et al. 2016, *ApJ*, 826, 159, doi: [10.3847/0004-637X/826/2/159](https://doi.org/10.3847/0004-637X/826/2/159)
- Stierwalt, S., Armus, L., Charmandaris, V., et al. 2014, *ApJ*, 790, 124, doi: [10.1088/0004-637X/790/2/12410.48550/arXiv.1406.3891](https://doi.org/10.1088/0004-637X/790/2/12410.48550/arXiv.1406.3891)
- Sun, Y., Lyu, J., Rieke, G. H., et al. 2025, *ApJ*, 978, 98, doi: [10.3847/1538-4357/ad973b](https://doi.org/10.3847/1538-4357/ad973b)
- Tacchella, S., Conroy, C., Faber, S. M., et al. 2022, *ApJ*, 926, 134, doi: [10.3847/1538-4357/ac449b](https://doi.org/10.3847/1538-4357/ac449b)
- Tielens, A. G. G. M. 2008, *Annu. Rev. Astron. Astrophys. Vol 46 P 289-337* 2008, 46, 289, doi: [10.1146/annurev.astro.46.060407.145211](https://doi.org/10.1146/annurev.astro.46.060407.145211)
- Tielens, A. G. G. M., & Hollenbach, D. 1985, *ApJ*, 291, 722, doi: [10.1086/163111](https://doi.org/10.1086/163111)
- Topping, M. W., Shapley, A. E., Sanders, R. L., et al. 2021, *MNRAS*, 506, 1237, doi: [10.1093/mnras/stab1793](https://doi.org/10.1093/mnras/stab1793)
- Tran, K.-V. H., Forrest, B., Alcorn, L. Y., et al. 2020, *ApJ*, 898, 45, doi: [10.3847/1538-4357/ab8c8a](https://doi.org/10.3847/1538-4357/ab8c8a)
- Treyer, M., Schiminovich, D., Johnson, B. D., et al. 2010, *ApJ*, 719, 1191, doi: [10.1088/0004-637X/719/2/1191](https://doi.org/10.1088/0004-637X/719/2/1191)
- U, V., Sanders, D. B., Mazzarella, J. M., et al. 2012, *ApJSuppl. Ser.*, 203, 9, doi: [10.1088/0067-0049/203/1/9](https://doi.org/10.1088/0067-0049/203/1/9)
- Urrutia, T., Wisotzki, L., Kerutt, J., et al. 2019, *A&A*, 624, A141, doi: [10.1051/0004-6361/201834656](https://doi.org/10.1051/0004-6361/201834656)
- Virtanen, P., Gommers, R., Oliphant, T. E., et al. 2020, *Nature Methods*, 17, 261, doi: [10.1038/s41592-019-0686-2](https://doi.org/10.1038/s41592-019-0686-2)
- Walter, F., Decarli, R., Aravena, M., et al. 2016, *ApJ*, 833, 67, doi: [10.3847/1538-4357/833/1/67](https://doi.org/10.3847/1538-4357/833/1/67)
- Werner, M. W., Roellig, T. L., Low, F. J., et al. 2004, *ApJS*, 154, 1, doi: [10.1086/422992](https://doi.org/10.1086/422992)
- Whitaker, K. E., Kriek, M., van Dokkum, P. G., et al. 2012, *ApJ*, 745, 179, doi: [10.1088/0004-637X/745/2/179](https://doi.org/10.1088/0004-637X/745/2/179)
- Whitaker, K. E., Pope, A., Cybulski, R., et al. 2017, *ApJ*, 850, 208, doi: [10.3847/1538-4357/aa94ce](https://doi.org/10.3847/1538-4357/aa94ce)
- Whitaker, K. E., Franx, M., Leja, J., et al. 2014, *ApJ*, 795, 104, doi: [10.1088/0004-637X/795/2/104](https://doi.org/10.1088/0004-637X/795/2/104)
- Whitaker, K. E., Ashas, M., Illingworth, G., et al. 2019, *ApJS*, 244, 16, doi: [10.3847/1538-4365/ab3853](https://doi.org/10.3847/1538-4365/ab3853)
- Whitcomb, C. M., Sandstrom, K., Leroy, A., & Smith, J.-D. T. 2022, *Star Formation and Molecular Gas Diagnostics with Mid- & Far-Infrared Emission*, arXiv. <https://arxiv.org/abs/2212.00180>
- Whitcomb, C. M., Smith, J.-D. T., Sandstrom, K., et al. 2024, *ApJ*, 974, 20, doi: [10.3847/1538-4357/ad66c8](https://doi.org/10.3847/1538-4357/ad66c8)
- Williams, C. C., Tacchella, S., Maseda, M. V., et al. 2023, *JEMS: A Deep Medium-Band Imaging Survey in the Hubble Ultra-Deep Field with JWST NIRC& NIRISS*, doi: [10.48550/arXiv.2301.09780](https://doi.org/10.48550/arXiv.2301.09780)
- Wright, G. S., Rieke, G. H., Glasse, A., et al. 2023, *PASP*, 135, 048003, doi: [10.1088/1538-3873/acbe66](https://doi.org/10.1088/1538-3873/acbe66)
- Wu, Y., Helou, G., Armus, L., et al. 2010, *ApJ*, 723, 895, doi: [10.1088/0004-637X/723/1/895](https://doi.org/10.1088/0004-637X/723/1/895)
- Wuyts, E., Wisnioski, E., Fossati, M., et al. 2016, *ApJ*, 827, 74, doi: [10.3847/0004-637X/827/1/74](https://doi.org/10.3847/0004-637X/827/1/74)
- Wuyts, S., Labbé, I., Förster Schreiber, N. M., et al. 2008, *ApJ*, 682, 985, doi: [10.1086/588749](https://doi.org/10.1086/588749)
- Wuyts, S., Förster Schreiber, N. M., Lutz, D., et al. 2011, *ApJ*, 738, 106, doi: [10.1088/0004-637X/738/1/106](https://doi.org/10.1088/0004-637X/738/1/106)
- Yan, L., Chary, R., Armus, L., et al. 2005, *ApJ*, 628, 604, doi: [10.1086/431205](https://doi.org/10.1086/431205)
- Zavala, J. A., Casey, C. M., Manning, S. M., et al. 2021, *ApJ*, 909, 165, doi: [10.3847/1538-4357/abdb27](https://doi.org/10.3847/1538-4357/abdb27)
- Zhang, J., Wuyts, S., Cutler, S. E., et al. 2023, *MNRAS*, 524, 4128, doi: [10.1093/mnras/stad2066](https://doi.org/10.1093/mnras/stad2066)
- Zhang, K., Yan, R., Bundy, K., et al. 2017, *MNRAS*, 466, 3217, doi: [10.1093/mnras/stw3308](https://doi.org/10.1093/mnras/stw3308)
- Zhu, Y.-N., Wu, H., Cao, C., & Li, H.-N. 2008, *ApJ*, 686, 155, doi: [10.1086/591121](https://doi.org/10.1086/591121)
- Zimmerman, D. T., Narayanan, D., Whitaker, K. E., & Davè, R. 2024, *Tracing the History of Obscured Star Formation with Cosmological Galaxy Evolution Simulations*, arXiv, doi: [10.48550/arXiv.2401.06719](https://doi.org/10.48550/arXiv.2401.06719)